

# Geochemistry, Geophysics, Geosystems

## RESEARCH ARTICLE

10.1029/2018GC007692

### Special Section:

Carbon degassing through volcanoes and active tectonic regions

### Key Points:

- We present high-resolution gas compositional data acquired using a multirotor Unmanned Aerial System (UAS) at Volcán Villarrica, Chile
- We derive SO<sub>2</sub>, CO<sub>2</sub>, and H<sub>2</sub>O fluxes of ~162, ~150, and ~2850 t/day, respectively
- UAS gas measurements made in the young, undiluted plume reveal short-term periodic active degassing associated with audible gas exhalations

### Supporting Information:

- Supporting Information S1
- Data Set S1
- Data Set S2

### Correspondence to:

E. J. Liu,  
ejl54@cam.ac.uk

### Citation:

Liu, E. J., Wood, K., Mason, E., Edmonds, M., Aiuppa, A., Giudice, G., et al. (2019). Dynamics of outgassing and plume transport revealed by proximal unmanned aerial system (UAS) measurements at Volcán Villarrica, Chile. *Geochemistry, Geophysics, Geosystems*, 20, 730–750. <https://doi.org/10.1029/2018GC007692>












Received 21 MAY 2018

Accepted 26 DEC 2018

Accepted article online 28 DEC 2018

Published online 5 FEB 2019

## Dynamics of Outgassing and Plume Transport Revealed by Proximal Unmanned Aerial System (UAS) Measurements at Volcán Villarrica, Chile

Emma J. Liu<sup>1</sup> , Kieran Wood<sup>2</sup> , Emily Mason<sup>1</sup> , Marie Edmonds<sup>1</sup> , Alessandro Aiuppa<sup>3,4</sup> , Gaetano Giudice<sup>4</sup> , Marcello Bitetto<sup>3</sup> , Vincenzo Francofonte<sup>4</sup>, Steve Burrow<sup>2</sup>, Thomas Richardson<sup>2</sup> , Matthew Watson<sup>5</sup>, Tom D. Pering<sup>6</sup> , Thomas C. Wilkes<sup>6</sup> , Andrew J. S. McGonigle<sup>4,6,7</sup> , Gabriela Velasquez<sup>8</sup>, Carlos Melgarejo<sup>8</sup>, and Claudia Bucarey<sup>8</sup>

<sup>1</sup>Department of Earth Sciences, University of Cambridge, Cambridge, UK, <sup>2</sup>Department of Aerospace Engineering, University of Bristol, Bristol, UK, <sup>3</sup>Dipartimento DiSTeM, Università di Palermo, Palermo, Italy, <sup>4</sup>Istituto Nazionale di Geofisica e Vulcanologia, Sezione di Palermo, Palermo, Italy, <sup>5</sup>School of Earth Sciences, University of Bristol, Wills Memorial Building, UK, <sup>6</sup>Department of Geography, University of Sheffield, Winter Street, UK, <sup>7</sup>School of Geosciences, University of Sydney, Sydney, Australia, <sup>8</sup>Observatorio Volcanológico de los Andes del Sur (OVDAS), Red Nacional de Vigilancia Volcánica (RNVV), Servicio Nacional de Geología y Minería, Temuco, Chile

**Abstract** Volcanic gas emissions are intimately linked to the dynamics of magma ascent and outgassing and, on geological time scales, constitute an important source of volatiles to the Earth's atmosphere. Measurements of gas composition and flux are therefore critical to both volcano monitoring and to determining the contribution of volcanoes to global geochemical cycles. However, significant gaps remain in our global inventories of volcanic emissions, (particularly for CO<sub>2</sub>, which requires proximal sampling of a concentrated plume) for those volcanoes where the near-vent region is hazardous or inaccessible. Unmanned Aerial Systems (UAS) provide a robust and effective solution to proximal sampling of dense volcanic plumes in extreme volcanic environments. Here we present gas compositional data acquired using a gas sensor payload aboard a UAS flown at Volcán Villarrica, Chile. We compare UAS-derived gas time series to simultaneous crater rim multi-GAS data and UV camera imagery to investigate early plume evolution. SO<sub>2</sub> concentrations measured in the young proximal plume exhibit periodic variations that are well correlated with the concentrations of other species. By combining molar gas ratios (CO<sub>2</sub>/SO<sub>2</sub> = 1.48–1.68, H<sub>2</sub>O/SO<sub>2</sub> = 67–75, and H<sub>2</sub>O/CO<sub>2</sub> = 45–51) with the SO<sub>2</sub> flux (142 ± 17 t/day) from UV camera images, we derive CO<sub>2</sub> and H<sub>2</sub>O fluxes of ~150 t/day and ~2,850 t/day, respectively. We observe good agreement between time-averaged molar gas ratios obtained from simultaneous UAS- and ground-based multi-GAS acquisitions. However, the UAS measurements made in the young, less diluted plume reveal additional short-term periodic structure that reflects active degassing through discrete, audible gas exhalations.

## 1. Introduction

The gases released by volcanoes at the Earth's surface are a window into the magmatic systems beneath. Abrupt changes in gas composition have been shown to occur immediately prior to large “paroxysmal” eruptions at several arc volcanoes worldwide, with gas ratios such as CO<sub>2</sub>/SO<sub>2</sub> identified in hindsight as timely forecasts of shifts in eruptive behavior (Aiuppa et al., 2007; Aiuppa, Bertagnini, et al., 2010; Aiuppa, Burton, et al., 2010; Aiuppa, Fischer, et al., 2017; de Moor et al., 2016; Shinohara, 2005; Shinohara et al., 2008; Werner et al., 2008). Cyclical variations in gas flux, particularly when cross-correlated with other monitoring parameters such as seismicity or ground deformation, provide critical insight into the mechanisms governing the time scales of recurrent eruptive activity (Flower & Carn, 2015; Ilanko et al., 2015; Nicholson et al., 2013; Odbert et al., 2014; Tamburello et al., 2013; Werner et al., 2008) and the data required to test hypotheses generated by numerical conduit models (e.g., Costa et al., 2007). On geological time scales, quantification of degassing budgets on a regional- or global-scale offers important constraints on volatile cycling through the Earth system (Aiuppa, Bitetto, et al., 2017; Mason et al., 2017). However, there remain significant gaps in our global inventories of volcanic gas emissions, particularly for CO<sub>2</sub> and other species which usually require proximal sampling of a concentrated plume, for those volcanoes where the near-vent region is hazardous or inaccessible.

Measurements of volcanic gas emissions can be either direct or remote. Direct measurements requiring placement of an instrument close to the vent source by volcanologists are hazardous to acquire and the instruments may often be destroyed during eruptions (e.g., Aiuppa, Fischer, et al., 2017). However, the high gas concentrations and limited atmospheric entrainment in young, proximal plumes yield high quality data that record faithfully primary degassing processes at a temporal resolution approaching that of geophysical data ( $\leq 1$  Hz). Remote measurements, such as can be acquired using imaging or spectral techniques (e.g., UV/IR-cameras and COSPEC/scanning-differential optical absorption spectroscopy (DOAS)/FlySpec/mobile-DOAS, respectively), are typically performed several kilometers from the volcanic gas source and therefore pose little to no direct risk to volcanologists or equipment (e.g., Bluth et al., 2007; Edmonds et al., 2003; Galle et al., 2003; Holland et al., 2011; Horton et al., 2006; McGonigle et al., 2002, 2003; Moffat & Millan, 1971; Mori & Burton, 2006; Oppenheimer et al., 1998; Platt et al., 2018; Tamburello et al., 2012, 2013; Weibring et al., 1998; Wilkes et al., 2016). Note that, although significant progress has been made in the use of Light Detection And Ranging (LIDAR) for remote sensing of  $\text{CO}_2$  (Santoro et al., 2017),  $\text{SO}_2$  is currently the only gas species able to be measured routinely by remote methods due to its strong absorption at UV wavelengths and the negligible concentration in ambient air. Globally, volcanic  $\text{SO}_2$  emissions are routinely monitored from space using satellite-based instrumentation (such as the Ozone Monitoring Instrument), or by ground-based networks at specific volcanoes (for example, the NOVAC network; Galle et al., 2010). In contrast, data for other gas species such as  $\text{H}_2\text{O}$  and  $\text{CO}_2$  are lacking for many volcanic systems where proximal measurements are challenging, particularly in a monitoring capacity.

Unmanned Aerial Vehicles (UAVs) are now bridging the gap between direct and remote measurements by enabling proximal sampling from a safe and accessible distance. Recent developments in drone technology (in terms of both physical capability and user-accessibility) have been matched by a drive toward increasingly lightweight and compact sensor payloads, such that the resulting Unmanned Aerial Systems (UAS) are rapidly becoming “go-to” solutions for a wide range of volcanological applications. UAS are driving the greatest advances in those fields requiring either proximal measurements in extreme environments or large areal coverage, including lava flow mapping, constructing topographic models, and eruptive volume estimations (Darmawan et al., 2018; Favalli et al., 2018; Moussallam et al., 2016; Müller et al., 2017; Nakano et al., 2014; Turner et al., 2017), post-eruption visual observation (Koyama et al., 2013), thermal imaging (Di Stefano et al., 2018), aeromagnetic surveys (Hashimoto et al., 2014; Kaneko et al., 2011), DOAS traverses for  $\text{SO}_2$  flux determination, and volcanic gas measurements and sampling (Diaz et al., 2015; Di Stefano et al., 2018; McGonigle et al., 2008; Mori et al., 2016; Pieri et al., 2013; Rüdiger et al., 2018; Shinohara, 2013; Stix et al., 2018).

Plume compositions measured by UAS 1–2 km from the vent following the 2014 phreatic eruption of Mt. Ontake demonstrated a dominantly hydrothermal degassing source (low  $\text{SO}_2/\text{H}_2\text{S}$  molar ratios, combined with  $\text{SO}_2$  concentrations  $<1$  ppm) and were critical to safe monitoring of the post-eruptive state of the volcano (Mori et al., 2016). At Turrialba volcano, Costa Rica,  $\text{SO}_2$  concentrations measured by UAS in the dilute distal plume (up to 3 km from the vent, measuring 0.3–20 ppm  $\text{SO}_2$ ) were used to derive estimates of  $\text{SO}_2$  emission rates using an inverse Bayesian modeling approach incorporating meteorological wind fields (Xi et al., 2016). A recent comparison of  $\text{SO}_2$  fluxes obtained by traditional ground-based DOAS traverses to those from drone-mounted DOAS (DROAS) demonstrated the utility of UAS for this application, with the additional ability to constrain wind speeds at plume altitude based on passive drift speed of the UAS (Stix et al., 2018). Furthermore, comparison of  $\text{CO}_2/\text{SO}_2$  molar ratios obtained by ground-based multi-GAS and simultaneously by a UAS-based gas sensor unit at Masaya, Nicaragua (Rüdiger et al., 2018; Stix et al., 2018), showed that downwind measurements using UAS in dilute plumes yield robust correlations between gas species that are comparable to those derived from proximal ground-based measurements. However, molar ratios in distal plumes ( $<5$  ppm maximum  $\text{SO}_2$ ) can be characterized by larger standard deviations than proximal crater rim measurements ( $<38$  ppm  $\text{SO}_2$ ; Rüdiger et al., 2018), highlighting that, although feasible, challenges still remain in acquiring high quality data from dilute plumes. This is particularly true for gas species such as  $\text{CO}_2$ , which have much higher background concentrations in ambient air (e.g., Aiuppa et al., 2009). Recently, Rüdiger et al. (2018) demonstrate that UAS now enable the measurement of reactive halogen species in previously inaccessible downwind plume regions and present proof-of-concept data that suggest an interesting potential relationship between  $\text{Br}_x/\text{SO}_2$  and  $\text{CO}_2/\text{SO}_2$  at Stromboli, Italy.

In situ measurements of volcanic gas composition are particularly suited to a UAS-based approach as sampling young, high-temperature plumes minimizes the effects of atmospheric interactions that dilute and chemically modify the gas composition, and thus reduce the fidelity of the signal. Here we investigate short-timescale spatial and temporal variability in CO<sub>2</sub>, H<sub>2</sub>O, SO<sub>2</sub>, H<sub>2</sub>S, and HCl emissions within a very young plume at Volcán Villarrica, Chile. Villarrica is historically the most active volcano in Chile, and is one of only six volcanoes worldwide to host an open lava lake at its summit. It is a persistent emission source, and exhibited a notable compositional excursion in gas ratios prior to the last major eruption in March 2015 (Aiuppa, Fischer, et al., 2017). The accessibility to the open summit vent, together with the permanent multi-GAS instrument located on the crater rim for data comparison, makes Villarrica an ideal natural laboratory for UAS field testing. Specifically, we present UAS-measured gas molar ratios in combination with SO<sub>2</sub> flux estimates derived from remote UV camera measurements, to quantify periodicities in gas composition and flux (on time scales of tens of seconds to minutes). We describe the development and deployment of two instrumented UAS: a customized Vulcan Black Widow multirotor UAV carrying a live-telemetered multi-GAS payload, designed specifically to withstand challenging environmental conditions during static hovers in the concentrated plume, and a modular sensor attachment (Airgraph Aeris commercial prototype) to a DJI Phantom 3 Pro quadcopter offering agile mobility in the plume for large-scale SO<sub>2</sub> mapping.

The results presented in this study highlight previously unrecognized periodic degassing behavior at Volcán Villarrica and demonstrate further the validity of UAS for high-resolution studies and routine monitoring of volcanic emissions, more generally. Together with a suggested pre-flight checklist for UAV safe operation published as supporting information, this work contributes a solid foundation on which to further advance the use of UAS for volcanic gas sensing, with future research focused on achieving long-range missions (>3 km) and coordinated multi-UAS experiments at strongly degassing but inaccessible volcanoes.

## 2. Geological Setting

Volcán Villarrica (2,847 m AMSL) is a partially glaciated stratovolcano within the Southern Volcanic Zone (SVZ) of the Andes of Chile (Figure 1). The SVZ is a relatively carbon-poor volcanic arc segment compared to other arcs globally (Aiuppa, Bitetto, et al., 2017; Shinohara & Witter, 2005), with limited involvement of subducting slab-derived fluids in magma genesis (Jacques et al., 2013; Wehrmann et al., 2014). Villarrica's volcanic edifice hosts a persistently degassing open lava lake at its summit, which is periodically perturbed by Strombolian explosions and transient lava fountaining (Calder et al., 2004; Palma et al., 2008). Erupted magma compositions range from basaltic to basaltic andesite (50–57 wt% SiO<sub>2</sub>; Hickey-Vargas et al., 2004; Moreno et al., 1994; Witter et al., 2004), and include several mafic ignimbrites emplaced during Plinian eruptions during the Holocene (Costantini et al., 2011; Parejas et al., 2010). Historical eruptions, documented since 1558, have been predominantly characterized by mild/moderate explosive fountaining with occasional lava effusion. The surface of the lava lake fluctuates from <50 to >200 m below the crater rim on monthly time scales, and indicates the top of the magma column that resides in the main conduit (Calder et al., 2004; Moussallam et al., 2016; Palma et al., 2008; Richardson et al., 2014). Variations in lava lake level are broadly correlated with both seismicity and degassing flux: periods when the lava level is high in the conduit are typically associated with more vigorous bubble bursting activity, higher SO<sub>2</sub> fluxes, and elevated Real-time Seismic-Amplitude Measurement (RSAM) seismic amplitude (Palma et al., 2008).

Villarrica is a persistent emission source within the SVZ and has maintained an SO<sub>2</sub> flux on the order of a few hundred tons per day (t/day) during several campaign measurements since 2005 (Mather et al., 2004; Moussallam et al., 2016; Sawyer et al., 2011; Shinohara & Witter, 2005), and by a permanent DOAS network since 2010 maintained by the Observatorio Volcanológico de los Andes del Sur (OVDAS). From January 2010 through May 2012, the lava lake surface was continuously visible and SO<sub>2</sub> emission rates averaged 926 t/day (OVDAS, personal communication, April 1, 2018). Following subsidence of the lava lake out of view in June 2012, the emission rate reduced to an average of 386 t/day until February 2015 (OVDAS, personal communication). Prior to the paroxysmal eruption of 3 March 2015, volcanic infrasound signals recorded a rapid increase in the level of the magma free surface from a stable level at >120 m below the crater rim to <70 m in the days prior to the eruption (Johnson et al., 2018). Following the eruption, the lake level

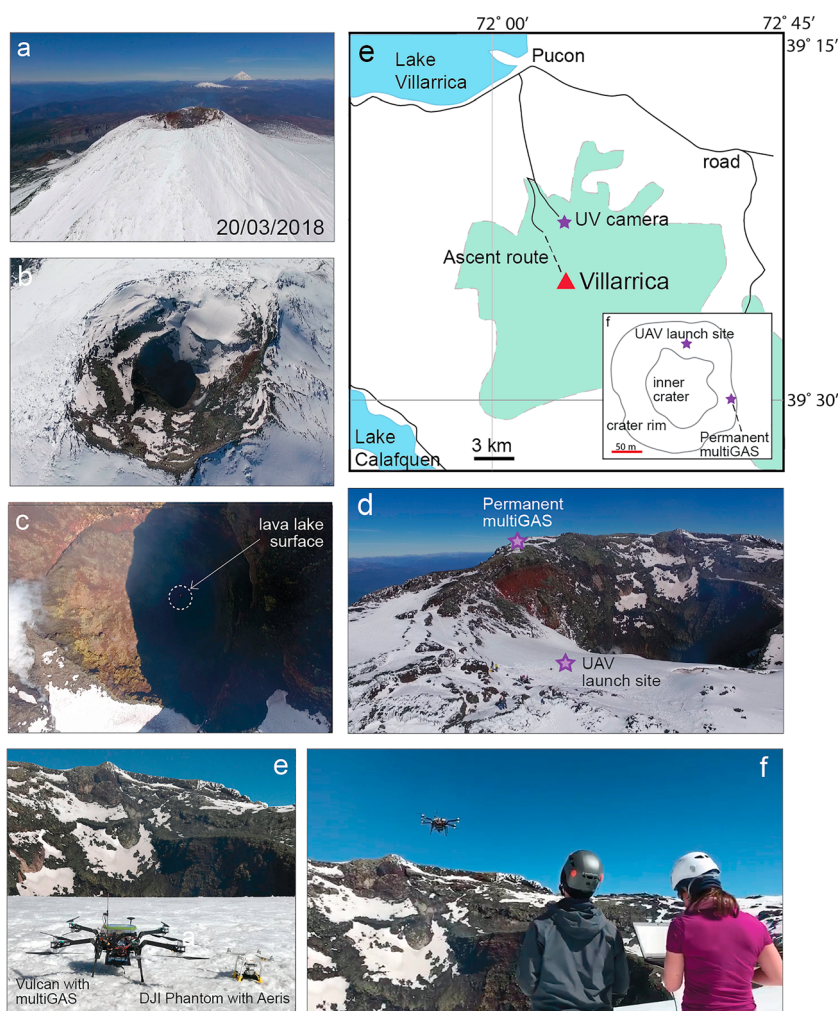


**Figure 1. Location and volcanological setting:** (a) Volcán Villarrica is the easternmost in a chain of three volcanoes (Lanin, Quetrapillan) striking obliquely to the main N-S axis of volcanism; (b, c) The magma level was extremely low in the conduit during the measurement campaign, with the lake surface only visible as several pixels in aerial imagery; (d) Unmanned Aerial Systems (UAS) were launched from a sheltered plateau on the northern rim of the crater, with the semipermanent multi-GAS station visible on the eastern rim; (e) location map of the region, showing the position of UV camera. The green shaded region delimits the extent of the national park. Inset: Aerial map of the summit region shown in (d). The summit crater is ~200 m in diameter; (e) Two instrumented multirotor vehicles were used in this campaign, the Vulcan octocopter with multi-GAS (left) and DJI Phantom 3 Pro with AERIS gas sensor (right); (f) Vulcan UAS in flight on 20 March 2018. UAV = Unmanned Aerial Vehicle.

remained high, maintaining an average  $\text{SO}_2$  flux of 714 t/day until December 2017 when the magma column again withdrew out of sight (OVDAS, personal communication).

A permanent, fully autonomous multi-GAS station installed on the eastern side of the summit crater detected a significant compositional excursion in molar gas ratios toward more  $\text{CO}_2$ -rich compositions immediately prior to the last major eruption in March 2015 (Aiuppa, Fischer, et al., 2017). Although the instrument was destroyed during the intense lava fountaining activity of 3 March, a replacement station was reinstalled in late November 2017, and acquires data during four 30-min sampling windows each day. Previous campaign measurements using ground-based multi-GAS instruments at Villarrica (Aiuppa, Fischer, et al., 2017; Moussallam et al., 2016; Shinohara & Witter, 2005) have not identified any clear periodic gas compositional variations associated with observed lava lake dynamics, but it remains unresolved whether this reflects the true degassing signature or is the result of homogenization and dilution during plume transport to the crater rim.



### 3. Methods

#### 3.1. UAS Design

Volcanic gas sensing requires a vehicle that is robust and resilient in the field, resists acid gas corrosion, and has sufficient propulsion and mobility to remain stable in strong winds. In response to these criteria, together with the need for modular attachment of sensor packages, we developed a bespoke UAS based on a multirotor platform. The multirotor configuration was selected over a fixed-wing design for this field campaign due to the need to maintain a static hover at a single position in the plume and to approach the vent in close proximity.

The vehicle was an octocopter in the X8 configuration based on a Vulcan “Black Widow” frame with hub-to-hub diameter of 120 cm (Vulcan UAV, United Kingdom). Lift was provided by eight 16-inch (407 mm) propellers with a hub-to-hub dimension of 140 cm. The mass of the frame, instrument payload, and batteries were 6.2, 0.8, and 3.5 kg respectively, resulting in a combined take-off weight of 10.5 kg. Maximum take-off weight is 16 kg. The vehicle used six 4,250 mAh capacity batteries, each with a nominal voltage of 24 V (6S). When testing at an altitude of 250 m AMSL prior to summit ascent, the vehicle comfortably achieved a 13-min flight duration with large capacity margins remaining in the battery. Given the performance degradation expected with the increased altitude (2,847 m) and wind speed at the summit, flight durations were conservatively limited to 13 min or until the battery voltage dropped below 22 V, whichever occurred sooner.

The avionics comprised several commercially available products, selected for their reliability and long-range capabilities. The flight computer is a Pixhawk 2.1 auto-pilot (Hex Technology, Hong Kong) with associated GPS module. All flight critical electronics were housed in sealed enclosures to reduce exposure to acidic volcanic gases and prevent corrosion. For the flight computer, a small hole was required in the case to allow for pressure equalization for the barometric altimeter, however the hole was sufficiently small to prevent significant airflow. Three separate radio-frequency links were used to communicate with the vehicle. The primary pilot control link used a transceiver set (Dragon Link, United States), operating on the 433 MHz frequency. An on-board video link used a transmitter and receiver set (ImmersionRC) on the 2.4 GHz frequency. The live video stream was made available to both the pilot and ground station via a first-person-view headset and handheld screen, thus allowing the vehicle to be visually positioned in the dense plume. The third link provided a stream of live flight data using RFD868+ radio modems (RFDdesign, Australia) operating on the 868 MHz frequency. Transmitted live data included information on the vehicle status, such as battery voltage and altitude, and real-time gas concentrations from the on-board multi-GAS sensor. The transmission of live sensor data to the ground station was achieved by transcoding the digital multi-GAS serial messages into the commonly used MAVLink protocol using a Teensy 3.6 microcontroller.

#### 3.2. Multi-GAS

Concentrations of CO<sub>2</sub>, SO<sub>2</sub>, and H<sub>2</sub>S (along with pressure, temperature, and relative humidity) were measured at a 1 Hz sampling rate within the volcanic plume using a miniaturized multicomponent gas analyzer (multi-GAS; see Table S1 for detailed specifications of all components; Aiuppa et al., 2007, 2009; Shinohara, 2005), customized to be flown on a multirotor UAS (section 3.1). The CO<sub>2</sub> spectrometer unit (non-dispersive infrared; NDIR) was wrapped in brass foil to shield the sensor board from radio-frequency interference from the UAS transmission system. H<sub>2</sub>O concentrations were calculated from records of temperature and relative humidity measured on-board the UAS, using a time-average pressure of  $724 \pm 0.5$  mbar. Air was sampled through a 1  $\mu$ m particle filter exposed to ambient air, at pump rate of 1.0 L/min. The multi-GAS was calibrated with standard reference gases at INGV Palermo 2 weeks prior to the field campaign, and again 2 weeks after. No significant sensor drift requiring data correction was identified. All sensor data were logged on-board, and also telemetered directly to the ground station where it could be visualized in real-time. Full specifications of the permanent ground-based multi-GAS station are given in Aiuppa, Bitetto, et al. (2017).

Multi-GAS concentration time series were post-processed using Ratiocalc software (Tamburello, 2015). CO<sub>2</sub> concentrations were corrected internally for temperature ( $\pm 0.2\%$  full span per degree Celsius) and pressure ( $\pm 0.15\%$  per hPa). No pressure correction was applied to SO<sub>2</sub> or H<sub>2</sub>S time series; however, applying the manufacturer compensation of 0.01% (SO<sub>2</sub>) and 0.008% (H<sub>2</sub>S) signal per mbar to a subset of the data shows a +2.9% increase in SO<sub>2</sub> concentrations (Figure S1; Kelly, 2017). This pressure effect translates to a maximum underestimation of 3.5 ppm at 120 ppm SO<sub>2</sub>, and <1 ppm underestimation at <35 ppm SO<sub>2</sub>. Importantly,

however, barometric pressure varied by  $<2$  mbar over the duration of the flight, so the temporal properties of the time series cannot be attributed to pressure fluctuations. Volcanogenic  $\text{CO}_2$  was resolved from atmospheric background by subtracting the  $\text{CO}_2$  concentration in ambient air ( $450 \pm 5$  ppmv; measured outside the plume where  $\text{SO}_2 = 0$ ) from the raw  $\text{CO}_2$  time series. No baseline drift correction was required for any gas species.  $\text{H}_2\text{S}$  concentrations were corrected for 13% cross-sensitivity to  $\text{SO}_2$  ( $\text{H}_2\text{S}_{\text{corrected}}$ ; Tamburello, 2015), where the magnitude of the cross-sensitivity was determined from laboratory tests using standard reference gases.

Molar ratios ( $\text{CO}_2/\text{SO}_2$ ,  $\text{H}_2\text{O}/\text{CO}_2$ , and  $\text{CO}_2/\text{H}_2\text{O}$ ) were derived from gas-gas scatterplots by calculating the gradient of the best-fit linear regression line through the data. Datapoints where  $\text{SO}_2$  is present at  $<5$  ppmv were excluded from the regression due to the greater error associated with very dilute plumes (e.g., Aiuppa et al., 2009); and  $>120$  ppm due to the breakdown of the calibration curve above this concentration (the specific  $\text{SO}_2$  sensor model used here is expected to exhibit a linear response in the  $0\text{--}100$  ppm  $\pm 20\%$  range). Uncertainties in derived molar gas ratios are  $\geq 6.4\%$  at  $>10$  ppm  $\text{SO}_2$  level and  $12.5\%$  at  $<10$  ppm  $\text{SO}_2$ , based on the results of laboratory tests (Figures S2 and S3). Uncertainties on derived  $\text{CO}_2$  and  $\text{H}_2\text{O}$  volatile fluxes are based on the propagation of errors from both the molar gas ratios and the UV camera-derived  $\text{SO}_2$  flux time series (see section 3.6), assuming a conservative uncertainty on the molar ratio at  $\pm 12\%$ .

### 3.3. Sensor Response Effects

During sampling and measurement, the sensors themselves act like filters and therefore the measured gas concentrations may be different from the true input signals, in particular if these undergo high frequency or rapid variations (Roberts et al., 2017). The results presented here should therefore be looked at in conjunction with knowledge of the dynamic response of the specific sensors and system integration used. During tests it was found that these can be modeled using characteristic delays in series with either a first-order or rate-limited response where the delay can be considered to be the physical time it takes for the gas signal to reach the sensor from the inlet. To characterize the sensors, we performed controlled step tests at INGV Palermo with the multi-GAS used in this study, during which the sensors were exposed to a range of known gas concentrations introduced “instantaneously” at known times. We then modeled the sensor response using simulated signals, to determine the best-fit delay and dynamic parameters (Figures S4a–S4d). For the current sensor configuration, it was found that the  $\text{SO}_2$  electrochemical sensor can be characterized by a delay of 3 s together in conjunction with a first-order response with a time constant of 3.5 s. The  $\text{CO}_2$  NDIR spectrometer can be best modeled with a rate-limited response of 35 ppm/s and a delay of 5 s.

The effect of the  $\text{SO}_2$  sensor is therefore to act as a low pass filter with a corner frequency of 0.29 rad/s (0.045 Hz), reducing measurements varying at high frequencies when compared to the true values. It can also be seen that the effective nonlinear rate limiting behavior of the  $\text{CO}_2$  NDIR will also reduce high frequency-varying measurements when compared to the true values. To demonstrate the effect of one of these sensors, we can consider the measured  $\text{SO}_2$  relative to the true values time series from Flight V1 to be the true, raw gas concentrations and pass them through the first-order model to derive the “filtered” time series. The output signal was then processed using RatioCalc in the same way as our measured data set (as described above) and we find that the measured  $\text{SO}_2$  signal is delayed and attenuated in amplitude by 7–30% (8–22 ppm; depending on duration of exposure to the peak concentration) relative to the input signal (Figures S4e–S4f). While theoretically it would be possible to retrieve additional amplitude and error information with regards to the original raw values using an inverse approach and with significant post processing of the results, this is beyond the scope of this paper and is the subject of ongoing work.

Instead, the different gas time series were harmonized by applying a Savitzky-Golay lowpass least-squares filter to the  $\text{SO}_2$  (13-point bandwidth, order 2) and  $\text{H}_2\text{O}$  (10-point bandwidth, order 2) time series, then determining the time offset required to maximize the correlation coefficient during linear regression with the unfiltered  $\text{CO}_2$  time series (Figure S5; Tamburello, 2015). The Savitzky-Golay filter was used specifically because it more effectively preserves peak height and width during noise reduction, which are usually attenuated by a moving average filter, however peak amplitudes can be degraded by  $\sim 5\%$  during harmonization. To further evaluate the error on the ratio resulting from differences in sensor response times (and thus the amplitude and width of peaks), the point-to-point regression-derived ratio was compared to that obtained by peak area integration, for each peak individually (Figure S6; Shinohara, 2005). Close agreement is observed

between the two methods, with the point-to-point regression typically yielding molar ratios  $\pm 4\%$  of the ratio derived from integration (Figure S6b).

### 3.4. Airgraph Aeris Gas Sensor Unit

SO<sub>2</sub>, H<sub>2</sub>S, and HCl concentrations (along with pressure, temperature, and relative humidity) were measured at a 1.25 Hz sampling rate within the volcanic plume using a commercial prototype Aeris gas analyzer (Airgraph Instruments, Australia; Figure 1e; see Table S1, for detailed specifications of all components) flown on a DJI Phantom 3 quadcopter UAV customized with a long-range transmission unit. The complete sensor package (including sensors, pump, tubing, outer casing, and wireless telemetry unit) has a mass of ~300 g and has been designed specifically to integrate with the Phantom series by clipping to the struts beneath the camera gimbal as a removable modular unit. The Aeris is controlled through an external laptop via a USB connection, which is then disconnected prior to takeoff once the Aeris has begun logging. All data are logged on-board and downloaded in the field by reconnection of the unit to the external laptop immediately after landing. The raw Aeris data were analyzed in the same manner as described above for multi-GAS data, using Ratiocalc software (Tamburello, 2015).

### 3.5. Field Deployment of UAS

We deployed the two gas analyzer-equipped UAS in the plume of Volcán Villarrica on 19 and 20 March 2018, as part of a longer field campaign at the same volcano spanning 13–27 March 2018 (Table S2). The wind speed on all other days of the field campaign were too high at the summit for additional flights. Full permissions for aerial work were obtained from the Chilean Dirección General de Aeronáutica Civil. Permissions were granted for line-of-sight operations within a specified area around the summit region, with a maximum flight altitude of 400 ft AGL. A copy of the pre-flight checklist is included in Text S1). This checklist was completed before every flight, and covers actions related to planning (e.g., defining a flight plan and objectives), ensuring the vehicle is flightworthy (e.g., battery and GPS checks), and recording relevant flight data to inform future operations (e.g., duration and battery usage). The checklist is not designed to be exhaustive and does not replace or ensure the competence of the operators, but rather mitigates against the risk of human error when operating in extreme environments. Although the checklist included in Text S1 is aimed at the UAS used in this study, many of the checks performed are applicable and transferable to UAS operations more generally.

The weather on both measurement days was clear, with very low humidity and wind speeds <10 m/s at summit altitude. The atmospheric conditions were thus extremely favorable for gas measurements and within the wind tolerance envelope for UAV flights. The UAS were launched from a plateau just inside the crater rim on the northern side of the summit, at an altitude of 2,850 m AMSL (Figure 1). Flight durations for the Vulcan multirotor ranged from 9 to 12 min. Average power consumption during flight was ~1,880 W. The UAS were operated within visual line of sight at all times, and due to the proximity of the plume to the take-off location the vehicle was manually piloted in the LOITER mode (GPS-assisted positioning). This mode provides position and orientation stability to automatically resist disturbances caused by wind or the turbulent plume. The multi-GAS and Aeris instruments were set to start logging up to 10 min prior to takeoff to allow sufficient time for the sensors to equilibrate and for the IR spectrometer to reach operating temperature (the warm-up time is 2 min, but stability continues to improve up to 30 min). Flight paths were specific to each UAS, and were chosen based on the scientific objective of each flight.

1. **Flight Objective 1—Plume mapping:** Gas concentrations in volcanic plumes are spatially heterogeneous due to a combination of both primary variability in degassing and interaction/entrainment with atmospheric air (Tamburello et al., 2012, 2013; Pering, Tamburello, McGonigle, Aiuppa, et al., 2014, and others). Plume identification was complicated further during our campaign because the plume was entirely noncondensing in the low humidity, and the extremely low level of the lava in the conduit meant the degassing source was not directly visible. To determine the most concentrated region of the plume for subsequent static hover flights, the Phantom-mounted Aeris sensor was flown in traverses across the crater, perpendicular to the wind direction, at approximately constant altitude to map out the typical cross-sectional structure of the volcanic plume within the Villarrica crater.
2. **Flight Objective 2—Static hover:** Temporal variations in volcanic gas flux and/or composition can provide insight into the nature of the degassing source, especially if these changes can be correlated with other observational variables. To measure a degassing time series, the Vulcan multirotor was deployed

to perform a static hover in the most concentrated part of the plume. The initial UAS positioning was chosen using the region of the highest gas concentration within Aeris plume maps and was further refined during flight in response to close monitoring of the live telemetry feed to maximize real-time measured concentrations.

### 3.6. PiCam UV Camera

The PiCam UV camera system uses two coaligned Raspberry pi cameras with horizontal field of view  $23.1^\circ$ , with optical filters (Edmund Optics Ltd.) centered at 310 ( $\text{SO}_2$  absorption) and 330 nm (no  $\text{SO}_2$  absorption; Wilkes et al., 2016, 2017). Images were taken at a frame rate of 0.125 Hz, using shutter speeds of 1,100/1,400 and 100 ms for the 310 and 330 nm filters, respectively. The UV camera was located directly north of the summit vent on 26 March 2018 ( $39^\circ 22' 38.64''\text{S}$ ,  $71^\circ 56' 46.99''\text{W}$ ),  $\sim 5.1$  km from the plume and perpendicular to the plume transport direction. Calibration was performed using three quartz cells containing known column amounts of  $\text{SO}_2$  ( $0$ ,  $304 \pm 31$  and  $1257 \pm 58$  ppm-m), and recalibrated every 90 min or whenever background conditions changed, whichever was sooner. The gas cell column amounts were measured independently using DOAS. Taking the largest cell uncertainty, we ascribe a  $\pm 10\%$  uncertainty to the calibration cell column amounts, based on 10 repeat measurements of each cell. Clear-sky images for vignette correction and dark images were also collected at these times.

Atmospheric conditions throughout acquisition were optimal for spectroscopic measurements, with a near-transparent, noncondensed plume with clear edge definition at all times and a cloud-free homogenous background. Errors resulting from light dilution (i.e., scattering of photons between the plume and the instrument within the field of view) are therefore dominated by the viewing distance and absolute  $\text{SO}_2$  integrated column amounts, and are likely toward the lower end of the 20–80% range of uncertainty demonstrated by Campion et al. (2015). Absolute scattering uncertainties could not be determined following the method of Campion et al. (2015), due to the presence of snow on the slopes. Furthermore, uncertainty arising from variations in the viewing distance cannot be fully quantified without exact independent knowledge of the plume position; however, we minimize this uncertainty by taking an integration line as close as possible to the edifice, which is of known distance at 5,100 m. We approximate this error using a value of  $\pm 500$  m (toward the upper end of potential variations given mitigations already in place), which translates to a  $\pm 10\%$  error in flux estimates.

Image sequences were post-processed using custom Python 3 software (including image alignment, vignette and dark image correction; Wilkes et al., 2016, 2017), before creation of absorption images (see Figure 5, for example). Plume speeds were calculated using the optical flow method (Peters et al., 2015; Peters & Oppenheimer, 2018) over cross-correlation, as motion estimation algorithms have been shown to yield more robust velocity estimates during benchmarking simulations (Peters et al., 2015), and to enable direct comparison with previous UV camera data from Villarrica (Peters et al., 2015; Moussallam et al., 2016). Calculated plume speeds range from 0.01 to 30 m/s with optical registration errors of 1.2% to 77% (however, 91% of the errors are  $<10\%$ , with a median error of 3.8%). The magnitude and variance of the errors are generally lower for higher plume speeds (Figure S7). To obtain a time series of  $\text{SO}_2$  flux (kg/s), plume speeds are multiplied by the corresponding integrated  $\text{SO}_2$  column amounts. For full details on protocols for UV camera measurement and post processing see Kantzas et al. (2010) and McGonigle et al. (2017). Combining the stated uncertainties associated with calibration, light scattering, viewing distance, and plume speed determination, we calculate a root-mean-square error on the derived  $\text{SO}_2$  fluxes of 12–41%.

### 3.7. Time Series Analysis

Volcanic systems, and open-vent volcanoes in particular, exhibit strongly periodic degassing behavior on a variety of time scales (e.g., Flower & Carn, 2015; Nicholson et al., 2013; Pering, Tamburello, McGonigle, Aiuppa, et al., 2014; Pering, Tamburello, McGonigle, Hanna, et al., 2014; Tamburello et al., 2012, 2013). The signals of multiple, superposed cycles within a time series can be deconvolved by spectral analytical approaches, such as Fast Fourier Transform (FFT) and Continuous Wavelet Transform (CWT), to reveal the frequency, and relative dominance, of underlying periodic components (e.g., Percival & Walden, 1993, 2006; Torrence & Compo, 1998). In this study, the cyclical character within time series of gas flux (UV camera) and concentration (multi-GAS) were quantified using both CWT and FFT methods. Prior to analysis, the time series were smoothed using a Savitzky-Golay filter (which minimizes the least-squares error in



polynomial fitting) and normalized to a zero-mean distribution. An additional requirement of FFT is that the time series are truncated to a length of  $2^n$  samples (for integer  $n$ ).

For FFT, Thompson's Multitaper Method (MTM) was implemented as it provides the most robust estimate of the power spectral density (PSD) at each frequency when there is no prior assumption of the signal generating source (Thompson, 1982). Statistical stationarity, required over the complete data window for MTM analysis, may not be appropriate for many geophysical systems known to exhibit temporal evolution in cyclic behavior; nonstationary yields broad undefined peaks in frequency spectra that are difficult to interpret, or masks the periodic component entirely. Moving-window FFT, where a series of PSD estimates are calculated using a shorter moving window of  $2^{(n-1)}$ , has been applied to volcanological data sets to account for temporal heterogeneity in the frequency domain (Lamb et al., 2014; Nicholson et al., 2013; Odbert & Wadge, 2009); however, this approach still requires the assumption of stationarity over the length of the moving window.

Wavelet analysis, here in the form of the CWT, offers additional degrees of freedom, such that not only can the requirement for stationarity be relaxed but the temporal persistence of cyclic components can be investigated in detail (e.g., Percival & Walden, 2006; Torrence & Compo, 1998). In comparison to FFT, which compares the signal to sine waves of different frequencies, wavelet transform compares the signal to scaled (dilation in the frequency domain) and shifted (translation in the time domain) versions of a "mother wavelet," for which the transform power at each time-frequency position can be visualized as a color-scaled scalogram. While sine waves are smooth and infinitely-repeating, wavelets are irregularly shaped and decay over a finite length; wavelets are therefore suited to analyzing unstable periodic phenomena or resolving discontinuities with high temporal localization. Here we compare our  $\text{SO}_2$  flux and concentration time series to the *Morlet* mother wavelet (which resembles a sine wave that decays with time away from its center) as it possesses many similarities to naturally occurring oscillations observed within the geosciences (Morlet et al., 1982; Odbert et al., 2014; Odbert & Wadge, 2009; Pering, Tamburello, McGonigle, Hanna, et al., 2014; Torrence & Compo, 1998). Edge effects resulting from the discrete nature of the time series may manifest as artificially high/low transform values in the CWT. The region of the CWT scalogram potentially affected by these edge effects is defined by the wavelet-specific cone-of-influence.

## 4. Results

### 4.1. Visual Observations

Throughout our measurement campaign the plume transport direction was toward the E to NE, consistent with the prevailing wind direction for the region and season, and was persistently fumigating the permanent multi-GAS station on the crater rim. The lava lake level was extremely low in the conduit, such that the free surface was not visible directly from the crater rim. Aerial observations using a UAV-mounted nadir camera showed the lava lake to comprise only a few pixels of the image (Figure 1c), confirming that the top of the magma column was residing several hundred meters below the summit elevation. We observed near-continuous passive degassing during a total of 18 hr (cumulative) spent at the summit, punctuated by active degassing pulses associated with audible gas exhalations (bubble bursts) from the lava lake below. Each audible exhalation lasted between 1 and 5 s (with the longer events comprising multiple discrete bursts) and was followed approximately 10 s later by the appearance of a buoyantly rising gas plume at the top of the conduit. The plume rose vertically above the vent until approximately level with crater rim, after which it began to interact with atmospheric winds and move laterally and more turbulently.

Active degassing, in the form of discrete gas exhalations, was clearly observed during our instrumented UAS flights and manifested in several quantifiable parameters in addition to the live-telemetered gas concentration. The arrival of each pulse of gas at the UAS was immediately accompanied by an abrupt increase in both hover turbulence and ambient temperature.

### 4.2. Compositional Mapping Through a Plume Cross-Section

The spatial distributions of  $\text{SO}_2$ ,  $\text{H}_2\text{S}$ , and  $\text{HCl}$  within a 2-D cross-section perpendicular to the plume transport direction were acquired during two flights on 20 March 2018 (P3, P4; Table S2) and a further flight on 21 March 2018 (P5). Sampling locations from the two flights on 20 March 2018 are displayed as a GoogleEarth overlay according to the GPS position of the UAS at the time of measurement and colored according to measured gas concentrations (Figure 2). All flights were approximately 15 min in duration, and therefore the

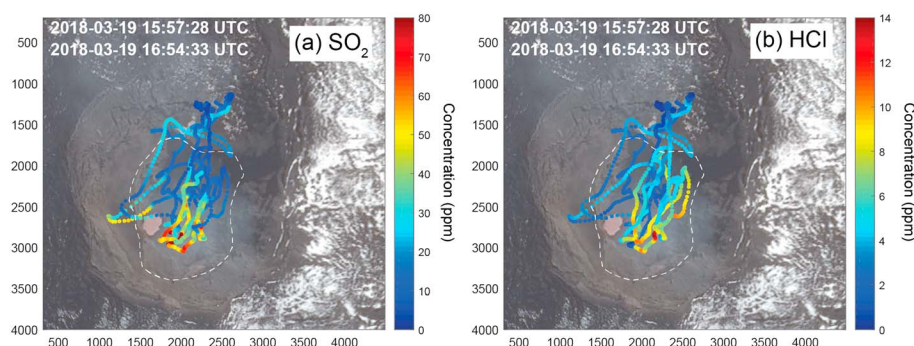


**Figure 2.** Cross-sectional plume maps of (a)  $\text{SO}_2$  and (b)  $\text{HCl}$  concentrations measured between 15:57 and 16:54 UTC on 20 March 2018. Each datapoint represents a discrete gas measurement every 0.8 s, positioned using corecorded GPS location and colored according to concentration. Dashed lines delimit the crater area.

maps shown in Figure 2 combine measurements acquired over  $\sim 30$  min. Although time-averaging in this way precludes identification of short-term temporal variations, the overall spatial distribution of degassing sources is likely to have remained relatively constant during the time interval of acquisition. The concentrations of all gas species are clearly elevated within a region in the S-SSE of the crater area, suggesting that this is the densest part of the plume and thus providing the target for the static hover UAS missions.  $\text{H}_2\text{S}$  concentrations were below the 13% cross-sensitivity to  $\text{SO}_2$  and are therefore not shown on Figure 2. The temporal superposition of concentrated gas pulses on dilute passive degassing may explain why some locations with overlapping transects have such contrasting concentrations.

#### 4.3. Molar Gas Ratios

Elevated concentrations of  $\text{CO}_2$ ,  $\text{SO}_2$ , and  $\text{H}_2\text{O}$  relative to atmospheric background were encountered throughout UAS hover flights (V1 and V2; Table S2; Figure 3).  $\text{H}_2\text{S}$  concentrations were below the 13% cross-sensitivity to  $\text{SO}_2$  with the exception of a single peak ( $>100$  ppmv  $\text{SO}_2$ ) where the  $\text{SO}_2/\text{H}_2\text{S}_{\text{corrected}}$  ratio was 0.08, which we take to represent the lower limit on this molar ratio.  $\text{SO}_2$  concentrations span two orders of magnitude from  $<10^{-1}$  to  $>10^2$  ppmv. Peak concentrations during active degassing pulses occasionally exceeded the calibrated range of the electrochemical sensor, resulting in truncation of peak concentrations; saturated values  $>120$  ppmv were excluded from subsequent ratio calculations, but represent less than 5% of the data. Measured  $\text{CO}_2$  concentrations reached up to 987 ppmv, indicating volcanogenic contributions of  $\leq 450$  ppmv after subtracting ambient atmospheric background.

Temporal variations in  $\text{CO}_2$ ,  $\text{SO}_2$ , and  $\text{H}_2\text{O}$  yield good to very good statistical correlations between species (Figure 4; Table S3), and thus well-constrained molar gas ratios. We derived  $\text{CO}_2/\text{SO}_2$  ratios of  $1.48 \pm 0.06$  and  $1.68 \pm 0.03$ ,  $\text{H}_2\text{O}/\text{SO}_2$  ratios of  $67 \pm 1.85$  and  $75 \pm 1.74$ , and  $\text{H}_2\text{O}/\text{CO}_2$  ratios of  $44 \pm 0.9$  and  $51 \pm 1.49$  (Table S3; the quoted uncertainty is the 95% confidence interval of the regression), each for flights V1 and V2, respectively. We find that variability in molar gas ratios is related to plume density, such that  $\text{CO}_2/\text{SO}_2$  ratios are both elevated and more variable in dilute plumes ( $<20$  ppmv  $\text{SO}_2$ , where  $\text{SO}_2$  is taken as the “plume marker” due to the negligible content in ambient air). The effect of measurement uncertainty on  $\text{CO}_2/\text{SO}_2$  is amplified as the denominator approaches zero; however, we also acknowledge that diffuse  $\text{CO}_2$ -rich degassing from the crater rim may contribute to more variable molar ratios at low  $\text{SO}_2$  (Stix et al., 2018). In dense plume conditions ( $>20$  ppmv  $\text{SO}_2$ ), the  $\text{CO}_2/\text{SO}_2$  ratio converges and stabilizes at lower values approaching  $1.69 \pm 0.34$  (Figure S8).

$\text{H}_2\text{O}$  is well correlated with both  $\text{SO}_2$  and  $\text{CO}_2$ , despite being calculated entirely independently of both variables (e.g.,  $\text{H}_2\text{O}/\text{SO}_2 = 67$  and  $75$  for flight V1 and V2, respectively;  $R^2$  between 0.94 and 0.96). The strength of this correlation reflects the extremely low humidity conditions under which these data were acquired ( $\text{Rh} < 10\%$  at summit altitude). The plume was noncondensing and almost transparent throughout the measurement period, thus producing an exceptionally smooth  $\text{H}_2\text{O}$  trace with a high signal-to-noise ratio.

#### 4.4. $\text{SO}_2$ Flux

A time series of  $\text{SO}_2$  emission rates was derived from 3 hr 45 min of UV camera acquisition on 26 March 2018 ( $n = 1430$ ; Figure 5).  $\text{SO}_2$  flux ranged from 0 to 12.4 kg/s (17 to 1071 t/day) during the measurement period,

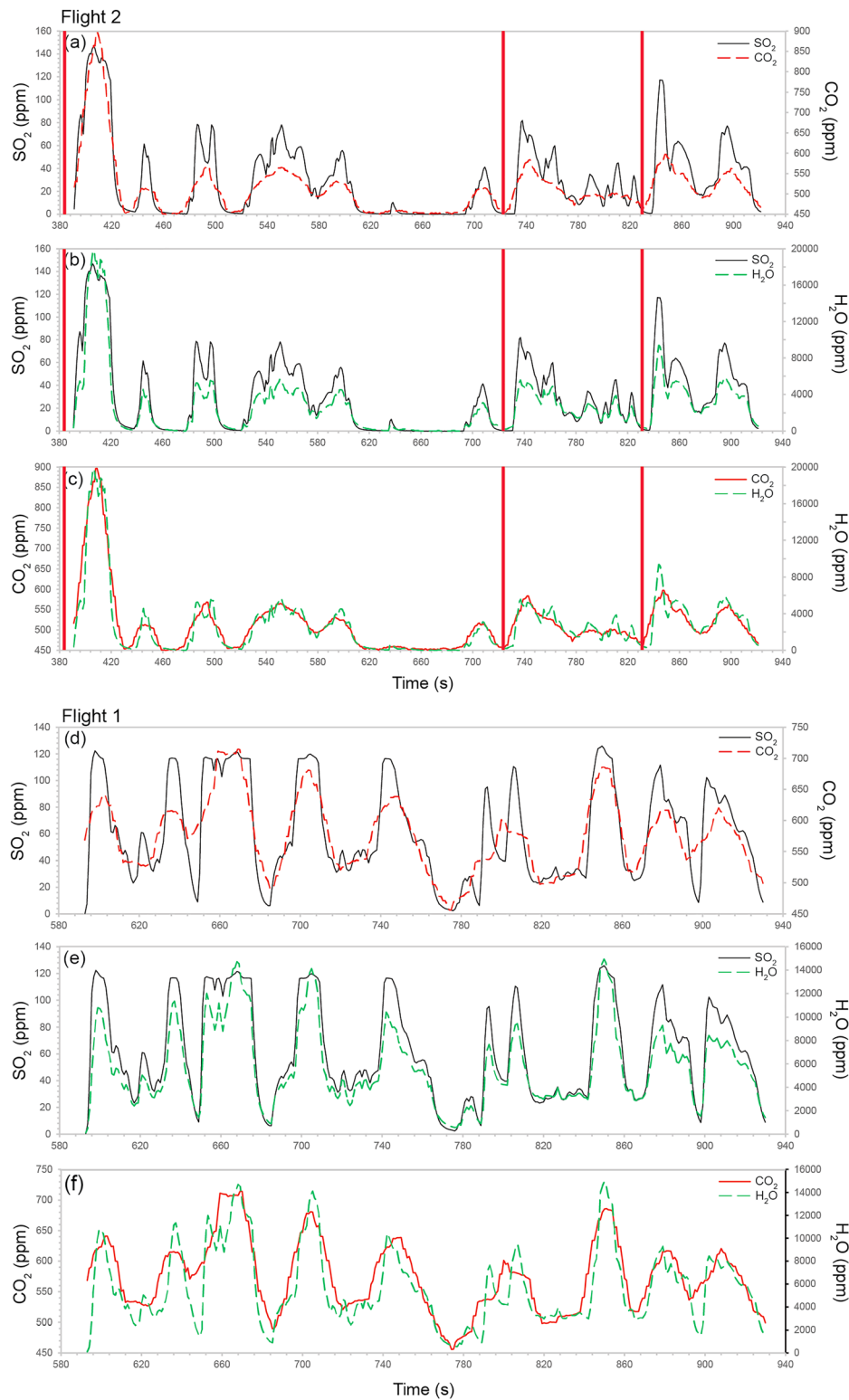


**Figure 3. Concentration time series for (a–c) multi-GAS Flight V1 at 16:49:00 UTC on 21 March 2018 showing covariation between multiple gas species; (a) SO<sub>2</sub> and CO<sub>2</sub>; (b) SO<sub>2</sub> and H<sub>2</sub>O; and (c) CO<sub>2</sub> and H<sub>2</sub>O. Measurement uncertainties on individual SO<sub>2</sub> and CO<sub>2</sub> values are 1 ppm ± 2% of the signal. Vertical red lines indicate the timing of audible gas exhalations recorded during the flight. Note that although the behavior was clearly heard and observed between flights, it was difficult to hear the exhalations above the motor noise from the Unmanned Aerial Vehicle, so many events were unrecorded. (d–f) Multi-GAS Flight V2 at 18:08:30 UTC on 21 March 2018 showing covariation between multiple gas species; (d) SO<sub>2</sub> and CO<sub>2</sub>; (e) SO<sub>2</sub> and H<sub>2</sub>O; and (f) CO<sub>2</sub> and H<sub>2</sub>O. Measurement uncertainties on individual SO<sub>2</sub> and CO<sub>2</sub> values are 1 ppm ± 2% of the signal.**

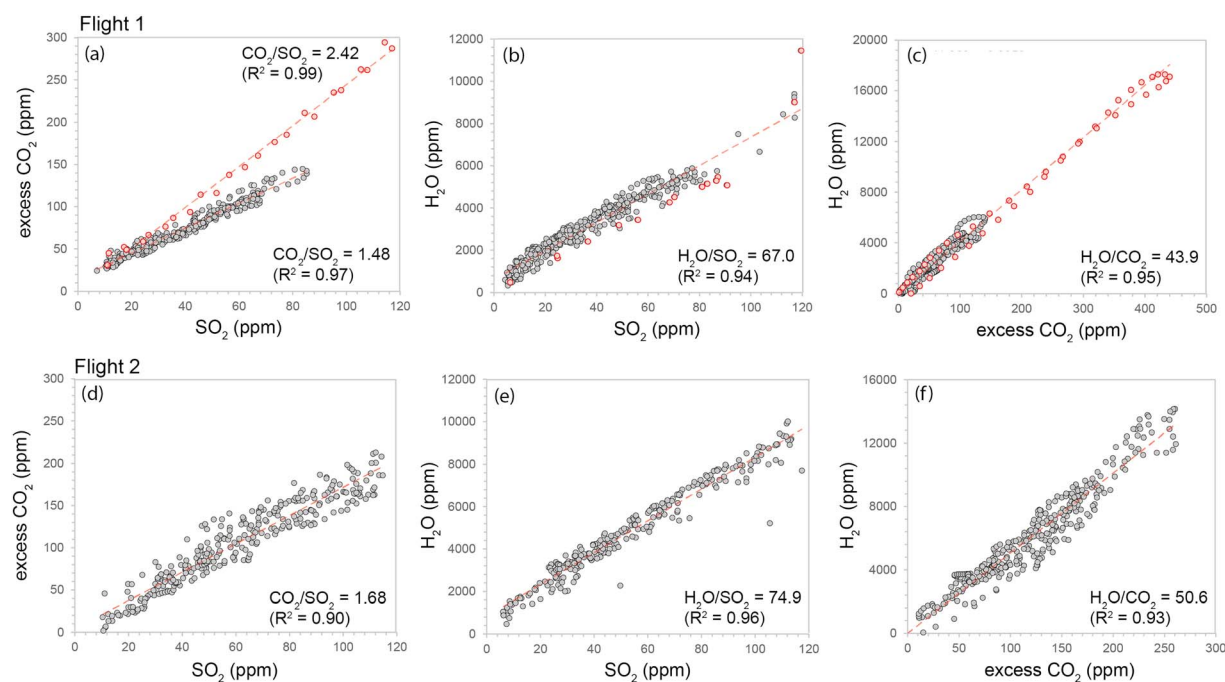


**Figure 4. Molar ratios of gas species** for (a–c) Flight V1 and (d–f) Flight V2. Ratios are determined from the slope of the best-fitting linear regression line. Only data where  $\text{SO}_2$  is  $>10$  and  $<120$  ppmv  $\text{SO}_2$  were used for the regression. Samples outside of these limits were excluded from the regression and are not displayed. Red symbols in (a–c) highlight an individual gas pulse that is characterized by an apparently more  $\text{CO}_2$ -rich composition. However, molar gas ratios are based on regression of the gray symbols only, as the anomalous gas pulse is not representative of the degassing characteristics during the measurement interval. Uncertainties on derived molar ratios are 6–12%, based on laboratory tests conducted at INGV Palermo.

with a median flux of  $1.64 \pm 0.2$  kg/s ( $142 \pm 17$  t/day; the quoted uncertainty represents the root-mean-square error at  $\pm 12\%$ , please see section 3 for a discussion of the main sources of uncertainty). Median plume speeds calculated for each acquisition period individually are  $4.33 \pm 0.2$  (section 1b) and  $7.12 \pm 0.3$  m/s (section 2), yielding median fluxes of  $1.54 \pm 0.2$  (section 1b) and  $1.90 \pm 0.2$  kg/s (section 2), respectively. Note that the PiCam was recalibrated between sections 1 and 2.

Periodic degassing behavior was noted in the field, and is clearly visible in the absorbance images and flux time series. An animated GIF of absorbance images from first half of section 2 provides a visual representation of the pulsatory behavior (Video S1). An individual  $\text{SO}_2$  pulse is magnified in Figure 5b, together with pseudocolor images of  $\text{SO}_2$  integrated column amounts corresponding to specific annotated positions on the flux time series (Figures 5c–5g). The  $\text{SO}_2$  flux is positively correlated with the calculated plume speed, such that peaks in  $\text{SO}_2$  flux reflect discrete, buoyant gas-rich exhalations.

## 5. Discussion

### 5.1. Volatile Fluxes

The molar plume compositions are comparable between the two flights: 96.4 ( $\text{H}_2\text{O}$ ), 2.13 ( $\text{CO}_2$ ), and 1.44 mol% ( $\text{SO}_2$ ) for flight V1 and 96.6 ( $\text{H}_2\text{O}$ ), 2.17 ( $\text{CO}_2$ ), and 1.29 mol% ( $\text{SO}_2$ ) for flight V2. Combining in-plume molar gas ratios (converted to mass ratios) with the time-averaged  $\text{SO}_2$  flux derived from remote UV camera measurements, we estimate the mass flux of  $\text{CO}_2$  and  $\text{H}_2\text{O}$  (Table S4). For a median  $\text{SO}_2$  flux of  $1.64 \pm 0.2$  kg/s (Figure 5) and the molar ratios shown in Table S3, we calculate emission rates of  $1.68 \pm 0.3$  and  $1.89 \pm 0.3$  kg/s ( $144 \pm 24$  and  $163 \pm 28$  t/day) for  $\text{CO}_2$ , and  $30.6 \pm 5.2$  and  $34.5 \pm 5.9$  ( $2,670 \pm 453$  and  $2981 \pm 506$  t/day) for  $\text{H}_2\text{O}$ , each for flights V1 and V2, respectively. Calculated plume compositions from this study are almost identical to those determined previously by Shinohara and Witter (2005)—95 mol%  $\text{H}_2\text{O}$ , 2.0 mol%  $\text{CO}_2$ , 2.1 mol%  $\text{SO}_2$ ,  $<0.01$  mol%  $\text{H}_2\text{S}$ , and 0.63 mol%  $\text{HCl}$ —thus, highlighting a remarkable stability in the composition of the gas phase outgassed during “background” activity at Villarrica over decadal time scales. The low molar proportion and flux of  $\text{CO}_2$  (e.g., compared to the



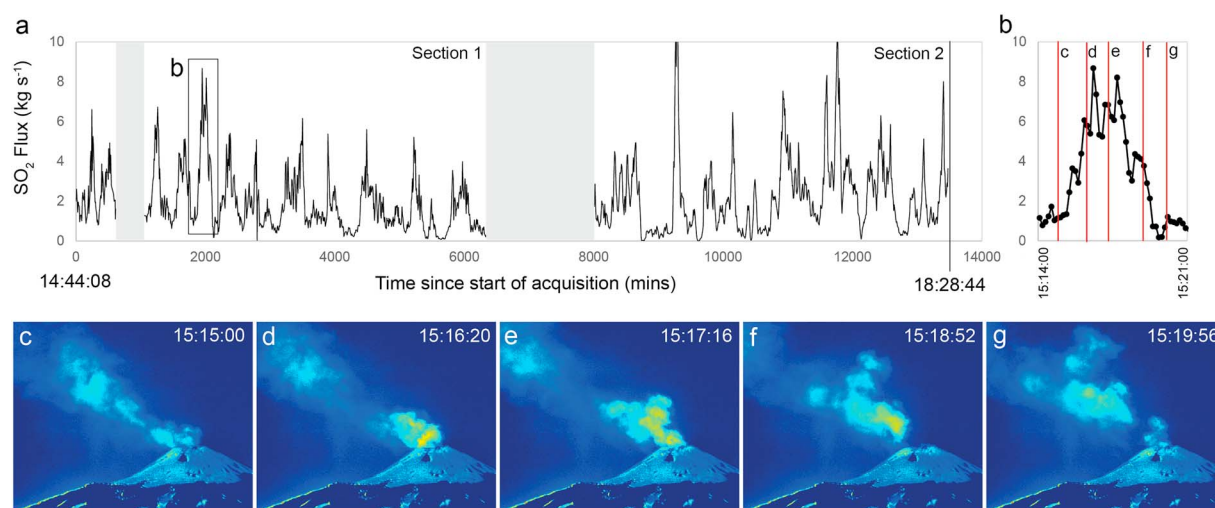


**Figure 5. SO<sub>2</sub> flux time series;** (a) time series of SO<sub>2</sub> flux from 14:44:04 to 18:28:44 UTC (3 hr 45 min) on 25 March 2018, derived from UV camera-generated integrated column amounts multiplied by plume speeds calculated using optical flow algorithms (Peters et al., 2015). Shaded regions correspond to breaks in acquisition during recalibration of the camera; (b) magnified view of a section of the SO<sub>2</sub> flux time series showing an individual gas “puff”; (c–g) time-stamped absorbance images showing the evolution of an individual gas puff. The acquisition times of the images (c–g) correspond to the red vertical lines displayed on (b).

28,50–3,900 t/day CO<sub>2</sub> emitted at Etna, Italy; Santoro et al., 2017) are consistent with the overall carbon-poor character of the SVZ.

The SO<sub>2</sub> flux during this campaign ( $142 \pm 17$  t/day) is within the range of previous flux measurements at Villarrica, which range from 40 to >1,000 t/day (Mather et al., 2004; Moussallam et al., 2016; Palma et al., 2008; Shinohara & Witter, 2005). On time scales of weeks to months the SO<sub>2</sub> flux appears to be strongly coupled to the lava lake dynamics, such that periods of elevated seismicity where the lava lake surface is at a high level in the conduit are associated with stronger SO<sub>2</sub> degassing (Palma et al., 2008). Campaign measurements between 2000 and 2006 show that emissions during low level background activity are characterized by a relatively constant flux on the order of a few hundred tons per day SO<sub>2</sub> (150–500 t/day), with rare transient excursions to higher values (up to ~1,000 t/day; e.g., January 2005; Palma et al., 2008). Most recently, Moussallam et al. (2016) reported SO<sub>2</sub> emission rates between 40 and 260 t/day from high-resolution UV camera images (during 1 hr of acquisition on 9 February 2016), with an average value of 160 t/day. At the time of measurements in February 2016, the lava lake level was low in the conduit (~140 m below the crater rim), with exposed surface area of ~700 m<sup>2</sup> (Moussallam et al., 2016). The state of the lava lake was therefore comparable to that observed during the present study, although we estimate the lava lake level in March 2018 to have been deeper (>200 m below the crater rim), and characteristic of background activity.

## 5.2. Comparison of UAS- and Ground-Based Multi-GAS Measurements

The second UAS flight (V2) was timed to coincide with the 30-min acquisition window (18:05–18:35 UTC) of the ground-based semiautonomous multi-GAS station located on the eastern side of the crater rim. Using SO<sub>2</sub> as the plume marker due to the negligible concentration in ambient air, Figure 6 shows that the concentrations measured by the UAS are an order of magnitude higher than those detected by the crater rim station, despite being located only ~100 m apart. SO<sub>2</sub> concentrations reaching the crater rim multi-GAS did not exceed 10 ppm on either of the measurement days, yet concentrations in excess of 100 ppm were routinely detected by the UAS-multi-GAS during gas pulses (Figure 6a). When displayed on different y axis scales to expand the detail within the crater rim multi-GAS time series, we observe little similarity between the two concentration traces (Figure 9b). This result is not unexpected, as we clearly observed in the field that as the plume exited the conduit it very quickly became dispersed by turbulent wind eddies within the crater region. This turbulence would quite effectively have homogenized the plume over the 10–15 s transport time required to travel 100 m lateral distance assuming plume speeds of ~5 m/s (based on the median plume speed derived by applying an optical flow algorithm to successive UV camera images; section 3.6).

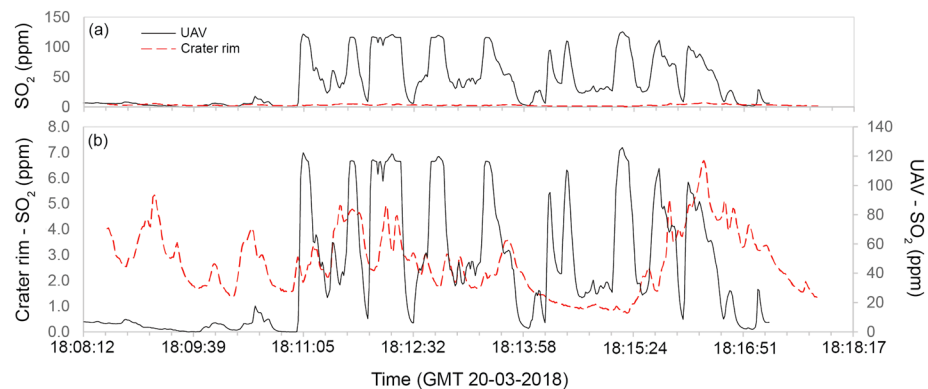


**Figure 6. Comparison between contemporaneous proximal UAV and crater rim SO<sub>2</sub> measurements;** (a) same scaled axis highlights the magnitude of plume dilution between the proximal measurements directly above the conduit and the crater rim only 100 m downwind; (b) time series displayed on individually scaled axes to compare the fine-scale detail. Even considering the temporal offset imposed by the downwind travel time, the periodic component of the proximal UAV trace is indistinguishable in the crater rim data.

Nevertheless, considering daily average molar ratios (which for the crater rim multi-GAS represent the average ratio measured over  $4 \times 30$  min intervals each day) we observe good agreement between the UAS-based and ground-based systems (Figure 7). Since installation of the crater rim multi-GAS station in early December 2017, CO<sub>2</sub>/SO<sub>2</sub> molar ratios spanning a range from  $<1$  to 15 have been reported. Elevated (but highly variable) CO<sub>2</sub>/SO<sub>2</sub> ratios  $>4$  (average:  $4.51 \pm 2.3 [1\sigma]$ ) were measured during the first section of the time series from 5–16 December 2017. After 16 December, ratios reduced abruptly and stabilized to values not exceeding 4. Over the period from 16 December to 25 March 2018, the average CO<sub>2</sub>/SO<sub>2</sub> ratio was  $2.46 \pm 0.9 [1\sigma]$ . The more CO<sub>2</sub>-rich gas compositions in early December occurred during a period of heightened activity, where the lava lake level was very high (Figure 7b), strong incandescence was recorded (Figure S9) and persistent MODIS satellite thermal anomalies were detected (MIROVA). During this period, vigorous bubble bursting and lava fountaining was observed from the crater rim and detected by the infrasound monitoring array, and RSAM seismicity was elevated (OVDAS Reporte Especial de Actividad Volcanica, 05 December 2017 09:50). The alert level at Villarrica was raised to yellow (from green) between 4 and 31 December. The marked decrease in the CO<sub>2</sub>/SO<sub>2</sub> ratio in mid-December occurred coincident with an abrupt depression of the lava level that resulted in the complete disappearance of the lava lake surface from view (Figure 7b) and the initiation of a hiatus in detectable thermal anomalies or incandescence (Figure S9). These observations are entirely consistent with previous studies at Villarrica, which have demonstrated not only a strong positive correlation between degassing and RSAM/lava level (Palma et al., 2008), but also distinct changes in gas composition toward more CO<sub>2</sub>-rich compositions during periods of heightened activity (Aiuppa, Fischer, et al., 2017).

During the measurement campaign for this study, the CO<sub>2</sub>/SO<sub>2</sub> ratio was particularly low and varied between 0.8 and 2.1, with an average of 1.5 (over four datapoints from 17 to 25 March 2018; Figure 7). These values show close correspondence with the molar CO<sub>2</sub>/SO<sub>2</sub> ratios of  $1.48 \pm 0.02$  and  $1.68 \pm 0.03$  obtained by the UAS-multi-GAS (flight V1 and V2, respectively). Unfortunately, it was not possible to compare H<sub>2</sub>O/SO<sub>2</sub> or H<sub>2</sub>O/CO<sub>2</sub> ratios as H<sub>2</sub>O can only be measured in dense plume conditions (due to the high background concentration in ambient air) and is therefore rarely resolvable at the ground-based station. The low CO<sub>2</sub>/SO<sub>2</sub> ( $<2$ ) molar gas ratios suggest that during background low level activity degassing (both active and passive) is being driven by gas bubbles that have remained coupled to the magma until shallow pressures in the range 0.1–5 MPa (assuming closed system degassing from 200 to 0.1 MPa; Aiuppa, Fischer, et al., 2017). In other words, the bubbles being actively outgassed at the surface have not separated from the magma during convective flow within the conduit, or at least not until near-surface conditions (Aiuppa, Bitetto, et al., 2017; Moussallam et al., 2016; Witter et al., 2004). This low pressure degassing contrasts with the situation during elevated activity, where the CO<sub>2</sub>-rich gas compositions suggest much deeper gas-melt equilibration, and thus more deeply sourced volatiles (Aiuppa et al., 2009; Aiuppa, Bertagnini et al., 2010; Aiuppa, Bitetto, et al., 2017).

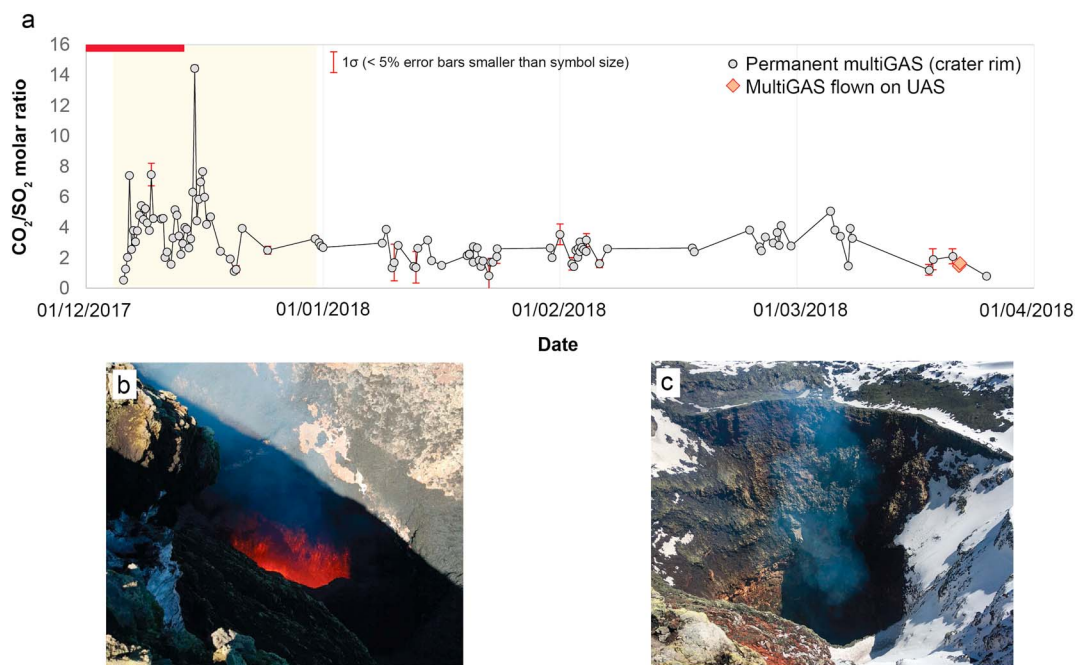


**Figure 7. Long-term time series of  $\text{CO}_2/\text{SO}_2$  molar ratios at Villarrica;** molar ratios are derived from raw  $\text{CO}_2$  and  $\text{SO}_2$  concentrations (measured by a permanent, automated multi-GAS station on the eastern crater rim of Villarrica; gray circles) using RatioCalc software (Tamburello, 2015); each datapoint represents the average  $\text{CO}_2/\text{SO}_2$  ratio within a 30-min acquisition window. Molar ratios derived from concentration time series acquired by the UAS-based multi-GAS are shown as orange symbols. Error bars represent the standard error of the regression for each acquisition window; errors  $<5\%$  are smaller than the size of the symbol. The shaded yellow region shows the period where the alert level defined by Observatorio Volcanológico de los Andes del Sur (OVDAS) was raised to yellow alert (from green). The red solid bar highlights the period where the lava lake surface was visible from the crater rim (b); it retreated abruptly below sight in mid-December 2017 (c). UAS = Unmanned Aerial Systems.

A single large bubble burst at the beginning of flight V1 (shown by the red symbols; Figures 4a–4c) is characterized by significantly higher  $\text{CO}_2/\text{SO}_2$  (and slightly reduced  $\text{H}_2\text{O}/\text{SO}_2$ ) compared to the tightly constrained bulk trend. The  $\text{CO}_2/\text{SO}_2$  ratio of 2.42 calculated for this individual peak by regression (or 2.75 by integration) suggests gas-melt equilibration under slightly higher pressures than the rest of the bubble population, toward the upper end of the 0.1–5 MPa range (Aiuppa, Fischer, et al., 2017).

### 5.3. Periodic Time Scales

The results obtained by applying wavelet analysis (continuous wavelet transform; CWT) and FFT to UAS-based  $\text{SO}_2$  concentrations are mutually consistent, and together indicate that the time series is composed of one or more periodic components superimposed on background noise (Figure 8). MTM power spectra for the two static hover flights (flights V1 and V2) indicate a strong shared frequency component at 0.023 Hz, which corresponds to a cycle period of  $\sim 44$  s (Figures 8c and 8d). Flight V1 contains a second, more dominant, cycle at 0.004 Hz, or  $\sim 250$  s. However, this component reflects the low concentration interval in the middle of the acquisition period, which imposes a symmetry to the time series that manifests as a cycle with wavelength equal to half the window length. With only two cycles within the complete data set we cannot determine if this low-frequency cycle is a true feature or simply an artifact of the data structure, and it will therefore not be considered further. Importantly, the broad spectral peaks suggest some degree of non-stationarity in the dominant frequency, with variability in the frequency domain that cannot be resolved by the fixed window length of FFT.

The CWT, expressed in the form of a scalogram, provides additional constraint on the time-frequency behavior (Figures 8a and 8b; note that the color-scale corresponds to different ranges of transform magnitude for each flight). For flight V2, the strongest correlation with the wavelet (i.e., the region of highest wavelet coefficients) is observed in the frequency range 23–28 mHz, equivalent to cycles 36–43 s in duration. Although

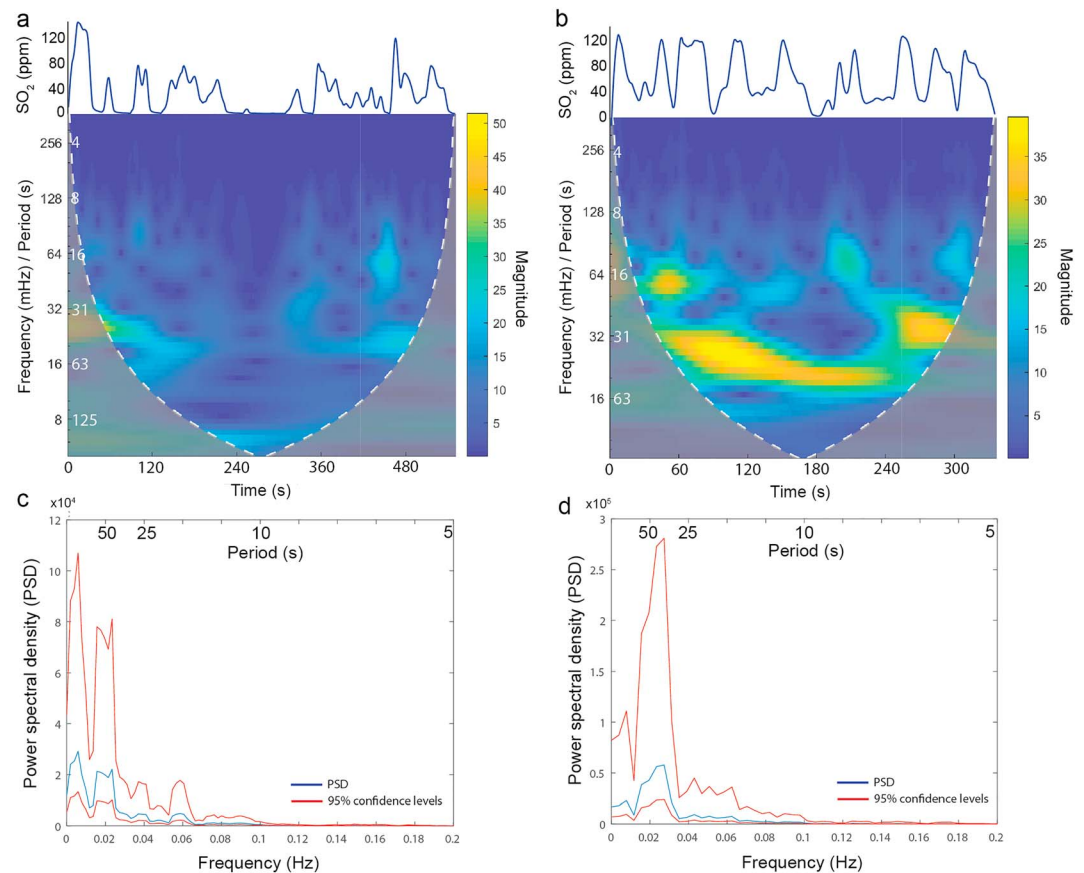


**Figure 8. Periodic behavior in  $\text{SO}_2$  concentration time series;** continuous wavelet transform scalograms for (a) Flights V1 and (b) V2, showing the magnitude of wavelet coefficients resulting from convolution of the  $\text{SO}_2$  time series with scaled (y axis) and shifted (x axis) versions of the Morlet wavelet. Note the different range of magnitudes shown by the color-scale for each flight. The shaded region represents the wavelet-specific cone-of-influence, which highlights the region of the continuous wavelet transform scalogram potentially affected by edge effects. The filtered time series of  $\text{SO}_2$  concentration is shown above for comparison; (c, d) Multitaper Method Fast Fourier Transform spectra showing the PSD at each frequency  $< 0.2$  Hz. The red lines indicate the upper and lower 95% confidence intervals. PSD = power spectral density.

this band of high coefficients is present throughout the time series (with time increasing left to right), the absolute frequency does not remain constant. The dominant frequency migrates from 35 mHz (29 s period) at 0–40 s to 20 mHz (49 s period) at 168–250 s. At 250 s, the dominant frequency returns abruptly to 35 mHz, and remains near this value for the remainder of the time series. The frequency glide reflects a progressive lengthening of the cycle period with time, and, together with the abrupt discontinuity at 250 s, confirms nonstationarity within the time series. Similarly, flight V1 also shows high transform power in the range 25–31 mHz (32–40 s period) at the beginning and end of the time series. However, the periodicity breaks down in the center of the time series, and instead becomes dominated by a low-frequency component at ~4 mHz (~250 s; see discussion above). The CWT scalograms agree well with the results from static PSD spectra in terms of absolute cycle frequency, while providing additional information related to the temporal persistence of each cycle.

There are several processes that could generate the observed periodic variation in  $\text{SO}_2$  concentration, including both primary (i.e., degassing dynamics) and secondary (e.g., atmospheric effects during transport from emission to the point of measurement) processes (Boichu et al., 2010). Transport effects within the crater itself include (a) local variability in wind speed, direction, or turbulence, which would modulate the degree of atmospheric entrainment and thus plume dilution, or (b) turbulent diffusion (i.e., generation of eddies by convection) and progressive large-scale organization of turbulence within the rising volcanic gas plume.



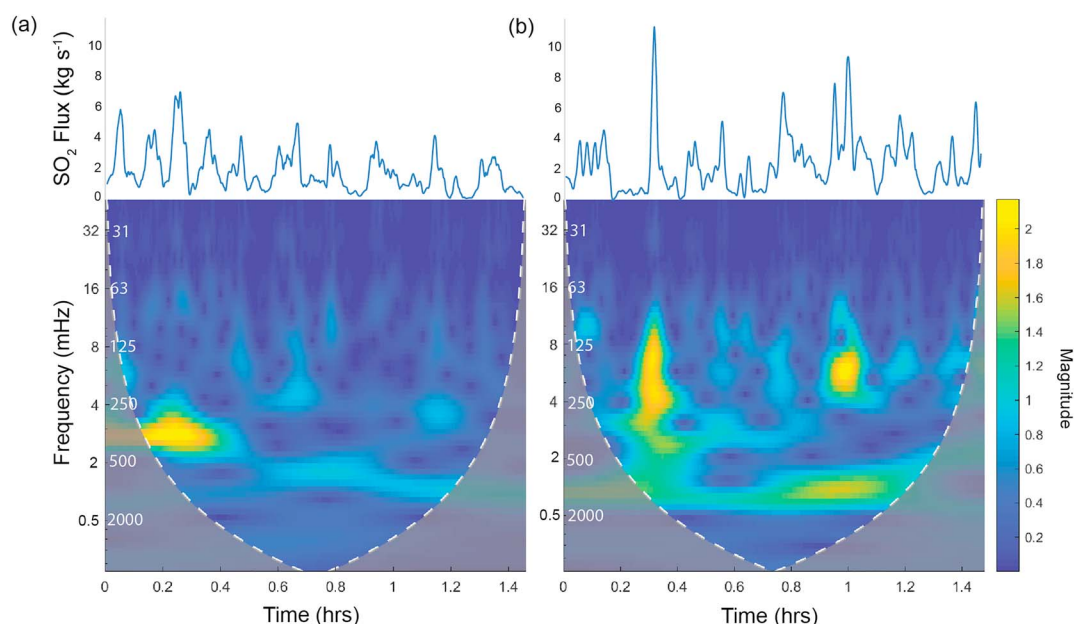


**Figure 9. Periodic behavior in  $\text{SO}_2$  flux derived from UV camera images;** continuous wavelet transform (CWT) scalograms for (a) section 2 and (b) section 3 of the  $\text{SO}_2$  flux time series (shown in Figure 8a) illustrating the magnitude of wavelet coefficients resulting from convolution of the flux time series with scaled ( $y$  axis) and shifted ( $x$  axis) versions of the Morlet wavelet. The filtered time series of  $\text{SO}_2$  flux is shown above for comparison. The shaded region represents the wavelet-specific cone-of-influence, which highlights the region of the CWT scalogram potentially affected by edge effects.

However, the onset of each peak in gas concentration (as observed in the live telemetry data) was preceded by an audible bubble burst  $\sim 10$  s prior to the emergence of a visible gas pulse appearing at the top of the conduit (vertical red lines on Figure 3 represent the timing of recorded bubble bursts but is not a complete data set) and an increase in thermal turbulence experienced by the UAS. Similar audible exhalations, followed by visible gas pulses, occurred regularly throughout the observation time spent at the summit region on time scales of tens of seconds to minutes (although repose times were not recorded explicitly). These observations suggest that the peaks in concentration, and thus the periodicity, are directly linked to active degassing dynamics, in the form of discrete bubble bursts at the surface of the lava lake.

The identification of distinct, and relatively persistent, short-term cycles (30–50 s) in the degassing time series stands in apparent contrast to previous studies where no periodic behavior was observed (Moussallam et al., 2016). These authors interpret the lack of structure in the gas signal to reflect turbulent mixing and homogenization between ascending, buoyant gas-rich magma and descending, dense, degassed magma in the conduit (Moussallam et al., 2016). We propose that the contrasting behaviors observed may reflect a difference in the outgassing regime between the two field campaigns. Although during the present study the surface of the lava lake could not be observed directly, the audible exhalations implied a small number of large bubble bursts (1–2 per minute). However, if many smaller bubbles were bursting more frequently (similar to the “seething magma” described by Palma et al., 2008) then one might expect the individual signature of each exhalation to be smaller in magnitude and superposed, thus producing an apparently structureless time series. We also note that while the UAS-based  $\text{SO}_2$  concentrations measured during flight V2 exhibit periodic behavior on time scales  $\sim 36$ – $43$  s, data acquired simultaneously by the ground-based multi-GAS on the crater rim show no such periodicity on any timescale (Figure 6b). Plume dilution and turbulent mixing in the atmosphere, even within the crater region, thus appear to effectively homogenize any short-term variability.

The  $\text{SO}_2$  flux time series derived from the remote UV camera images also displays strong periodic characteristics, but on significantly longer time scales than observed in the gas concentrations within the young plume. The early section of section 2 (Figure 9a) contains high transform power in the CWT scalogram centered on a frequency of 2.9 mHz (345 s/5.75 min period). With time, this cycle frequency gradually decreases

to reach  $\sim 1.4$  mHz (714 s/11.9 min period) where it once again stabilizes in the final third of the time series. Although each gas pulse visible in the absorption images appears to have an impulsive rise component to its motion (Video S1) suggesting a buoyant primary exhalation, we cannot exclude the possibility that this longer period cycle reflects large-scale organization of turbulence as the plume exits the crater and interacts with the atmosphere (Boichu et al., 2010). It is encouraging to see that even after pausing the acquisition, recalibrating, and restarting the UV camera (Figure 9b), section 3 of the  $\text{SO}_2$  time series contains the same low-frequency component ( $\sim 700$  s period) identified in the latter part of section 2, and thus transitions almost seamlessly from the previous scalogram. Abrupt increases in  $\text{SO}_2$  flux introduce sharp discontinuities into section 3 (most striking of which occurs at 0.35 hr). These discontinuities are clearly manifest in the scalogram as transient high transform values across all scales.

## 6. Summary and Conclusions

In this study, we demonstrate the efficacy of UAS-based gas measurements for investigating short-timescale variability in volcanic outgassing and plume transport processes, and for the derivation of well-constrained  $\text{CO}_2$  and  $\text{H}_2\text{O}$  fluxes, which necessitate high plume to background concentrations. To maximize the efficiency of field deployment, we find that mapping the plume with smaller, lighter UAS and then using these data to locate the static hover (refined further by live data telemetry) provides an effective operational approach that ensures rapid positioning within the region of maximum gas concentrations. Our data show that  $\text{SO}_2$  concentrations in the young proximal plume at Volcán Villarrica, Chile, exhibit periodic variations that are well correlated with other gas species. Derived molar gas ratios ( $\text{CO}_2/\text{SO}_2 = 1.48\text{--}1.68$ ,  $\text{H}_2\text{O}/\text{SO}_2 = 67\text{--}75$  and  $\text{H}_2\text{O}/\text{CO}_2 = 45\text{--}51$ ) are well-constrained with high statistical confidence. By combining in-plume molar gas ratios with the  $\text{SO}_2$  flux ( $142 \pm 17$  t/day) from UV camera images, we derive  $\text{CO}_2$  and  $\text{H}_2\text{O}$  fluxes of  $\sim 150$  and  $\sim 2,850$  t/day, respectively, consistent with the overall carbon-poor nature of magmas from the SVZ of the Andes (Shinohara & Witter, 2005; Aiuppa, Bitetto, et al., 2017).

Periodic variations are clearly evident in the gas concentration time series obtained during static hover flights. Cycle periods vary between 30 and 50 s (with the strongest periodicity manifest at 36–43 s), with marked nonstationarity over the duration of the time series, based on both wavelet and FFT analyses of the frequency content of the measured signal. Peaks in gas concentration were preceded by audible gas exhalations, thus suggesting that the periodicity reflects a primary degassing process (i.e., individual bubble bursts), rather than atmospheric effects during plume transport. Active degassing through discrete gas exhalations therefore provides an important contribution to outgassing at Villarrica that modulates gas flux over time scales of tens of seconds to minutes. UV camera-derived  $\text{SO}_2$  fluxes immediately above the summit crater are characterized by longer timescale periodicities (5–12 min), which likely reflect superposition of both primary degassing and large-scale organization of turbulence during the early phase of plume transport.

Simultaneous acquisitions by the UAS and a ground-based multi-GAS located on the crater rim highlighted that considerable plume dilution and homogenization occurs during transport within the crater, over horizontal length scales of only  $\sim 100$  m. UAS-based  $\text{SO}_2$  concentrations ( $< 120$  ppm) are generally an order of magnitude greater than measured at the crater rim ( $< 10$  ppm), and exhibit much more regular, short-timescale variability that can be correlated with discrete outgassing events. Despite this, time-averaged molar gas ratios obtained by the two multi-GAS systems are in good agreement and are consistent with a long-term decline in  $\text{CO}_2/\text{SO}_2$  following elevated levels of activity (and more  $\text{CO}_2$ -rich gas compositions) in December 2017. The present low  $\text{CO}_2/\text{SO}_2$  ratio  $< 2$  implies low pressure degassing in equilibrium with the shallow magma reservoir and is representative of background activity at Villarrica (Aiuppa, Fischer, et al., 2017). We therefore highlight the potential for UAS-based measurements to be applied in complement to ground-based gas monitoring at Villarrica, particularly when the lava lake is very low in the conduit and the crater rim station is typically sampling only a very dilute or aged plume.

## References

- Aiuppa, A., Bertagnini, A., Métrich, N., Moretti, R., Di Muro, A., Liuzzo, M., & Tamburello, G. (2010). A model of degassing for Stromboli volcano. *Earth and Planetary Science Letters*, 295, 195–204. <https://doi.org/10.1016/j.epsl.2010.03.040>
- Aiuppa, A., Federico, C., Giudice, G., Giuffrida, G., Guida, R., Gurrieri, S., et al. (2009). The 2007 eruption of Stromboli volcano: Insights from real-time measurement of the volcanic gas plume  $\text{CO}_2/\text{SO}_2$  ratio. *Journal of Volcanology and Geothermal Research*, 182, 221–230. <https://doi.org/10.1016/j.jvolgeores.2008.09.013>

## Acknowledgments

We are deeply grateful to both Richard and Coco of Sierra Nevada for their expert guiding during our multiple ascents of Villarrica, and their patience during many hours at the summit. We thank OVDAS for their collaboration and for liaising with CONAF for access permissions on our behalf, and Ángela Hernández (Centro de Investigación en Ecosistemas de la Patagonia) for assistance in obtaining flight permissions from the DGAC plus her support, along with Giovanni Denari (CIEP) and Alejandro Miranda (Universidad de la Frontera) during the initial ascent of the volcano. This work was directly funded by a Leverhulme Early Career Fellowship to E.J.L., and an EPSRC postgraduate studentship to E.M. T.R. and K.W. were supported by EPSRC through the CASCADE Programme grant (EP/R009953/1). T.D. P. acknowledges the support of the Royal Society (RG170226). I.M.W. was supported by NERC through the Centre for the Observation and Modeling of Earthquakes, Volcanoes, and Tectonics (COMET NE/J01978X/1). This research was supported through the Alfred P. Sloan Foundation's support of the Deep Carbon Observatory Deep Earth Carbon Degassing program (DECADE). We also thank Airgraph for the opportunity to be involved in the ongoing collaborative development and field testing of the Aeris. Raw data are available in the online supporting information.

- Aiuppa, A., Fischer, T. P., Plank, T., Robidoux, P., & Di Napoli, R. (2017). Along-arc, inter-arc and arc-to-arc variations in volcanic gas CO<sub>2</sub>/S<sub>T</sub> ratios reveal dual source of carbon in arc volcanism. *Earth-Science Reviews*, 168, 24–47. <https://doi.org/10.1016/j.earscirev.2017.03.005>
- Aiuppa, A., Moretti, R., Federico, C., Giudice, G., Gurrieri, S., Liuzzo, M., et al. (2007). Forecasting Etna eruptions by real-time observation of volcanic gas composition. *Geology*, 35, 1115–1118. <https://doi.org/10.1130/G24149A.1>
- Aiuppa, A., Bitetto, M., Francofonte, V., Velasquez, G., Parra, C. B., Giudice, G., et al. (2017). A CO<sub>2</sub>-gas precursor to the March 2015 Villarrica volcano eruption. *Geochemistry, Geophysics, Geosystems*, 18, 2120–2132. <https://doi.org/10.1002/2017GC006892>
- Aiuppa, A., Burton, M., Caltabiano, T., Giudice, G., Guerrieri, S., Liuzzo, M., et al. (2010). Unusually large magmatic CO<sub>2</sub> gas emissions prior to a basaltic paroxysm. *Geophysical Research Letters*, 37, L17303. <https://doi.org/10.1029/2010GL043837>
- Bluth, G. J. S., Shannon, J. M., Watson, I. M., Prata, A. J., & Realmuto, V. J. (2007). Development of an ultra-violet digital camera for volcanic SO<sub>2</sub> imaging. *Journal of Volcanology and Geothermal Research*, 161, 47–56. <https://doi.org/10.1016/j.jvolgeores.2006.11.004>
- Boichu, M., Oppenheimer, C., Tsanev, V., & Kyle, P. R. (2010). High temporal resolution SO<sub>2</sub> flux measurements at Erebus volcano, Antarctica. *Journal of Volcanology and Geothermal Research*, 190(3–4), 325–336. <https://doi.org/10.1016/j.jvolgeores.2009.11.020>
- Calder, E. S., Harris, A. J. L., Peña, P., Pilger, E., Flynn, L. P., Fuentealba, G., & Moreno, H. (2004). Combined thermal and seismic analysis of the Villarrica volcano lava lake, Chile. *Revista Geologica de Chile*, 31, 259–272. <https://doi.org/10.4067/S0716-02082004000200005>
- Campion, R., Delgado-Granados, H., & Mori, T. (2015). Image-based correction of the light dilution effect for SO<sub>2</sub> camera measurements. *Journal of Volcanology and Geothermal Research*, 300, 48–57. <https://doi.org/10.1016/j.jvolgeores.2015.01.004>
- Costa, A., Melnik, O., & Sparks, R. S. J. (2007). Controls of conduit geometry and wallrock elasticity on lava dome eruptions. *Earth and Planetary Science Letters*, 260, 137–151. <https://doi.org/10.1016/j.epsl.2007.05.024>
- Costantini, L., Pioli, L., Bonadonna, C., Clavero, J., & Longchamp, C. (2011). A Late Holocene explosive mafic eruption of Villarrica volcano, southern Andes: The Chaimilla deposit. *Journal of Volcanology and Geothermal Research*, 200, 143–158. <https://doi.org/10.1016/j.jvolgeores.2010.12.010>
- Darmawan, H., Walter, T. R., Brotopuspito, K. S., Subandriyo, & Nandaka, I. G. M. A. (2018). Morphological and structural changes at the Merapi lava dome monitored in 2012–15 using unmanned aerial vehicles (UAVs). *Journal of Volcanology and Geothermal Research*, 349, 256–267. <https://doi.org/10.1016/j.jvolgeores.2017.11.006>
- de Moor, J. M., Aiuppa, A., Avar, G., Wehrmann, H., Dunbar, N., Muller, C., et al. (2016). Turmoil at Turrialba volcano (Costa Rica): Degassing and eruptive processes inferred from high-frequency gas monitoring. *Journal of Geophysical Research: Solid Earth*, 121, 5761–5775. <https://doi.org/10.1002/2016JB013150>
- Di Stefano, G., Romeo, G., Mazzini, A., Iarocci, A., Hadi, S., & Pelphrey, S. (2018). The Lusi drone: A multidisciplinary tool to access extreme environments. *Marine and Petroleum Geology*, 90, 26–37. <https://doi.org/10.1016/j.marpetgeo.2017.07.006>
- Diaz, J. A., Pieri, D., Wright, K., Sorensen, P., Kline-Shoder, R., Arkin, C. R., et al. (2015). Unmanned aerial mass spectrometer systems for in-situ volcanic plume analysis. *Journal of the American Society for Mass Spectrometry*, 26(2), 292–304. <https://doi.org/10.1007/s13361-014-1058-x>
- Edmonds, M., Herd, R. A., Galle, B., & Oppenheimer, C. M. (2003). Automated, high time-resolution measurements of SO<sub>2</sub> flux at Soufrière Hills volcano, Montserrat. *Bulletin of Volcanology*, 65, 578–586. <https://doi.org/10.1007/s00445-003-0286-x>
- Favalli, M., Fornaciari, A., Nannipieri, L., Harris, A., Calvari, S., & Lormand, C. (2018). UAV-based remote sensing surveys of lava flow fields: A case study from Etna's 1974 channel-fed lava flows. *Bulletin of Volcanology*, 80, 29. <https://doi.org/10.1007/s00445-018-1192-6>
- Flower, V. J. B., & Carn, S. A. (2015). Characterising volcanic cycles at Soufrière Hills volcano, Montserrat: Time series analysis of multi-parameter satellite data. *Journal of Volcanology and Geothermal Research*, 304, 82–93. <https://doi.org/10.1016/j.jvolgeores.2015.07.035>
- Galle, B., Johansson, M., Rivera, C., Zhang, Y., Kihlman, M., Kern, C., et al. (2010). Network for Observation of Volcanic and Atmospheric Change (NOVAC)—A global network for volcanic gas monitoring: Network layout and instrument description. *Journal of Geophysical Research*, 115, D05304. <https://doi.org/10.1029/2009JD011823>
- Galle, B., Oppenheimer, C., Geyer, A., McGonigle, A. J., Edmonds, M., & Horrocks, L. (2003). A miniaturised ultraviolet spectrometer for remote sensing of SO<sub>2</sub> fluxes: A new tool for volcano surveillance. *Journal of Volcanology and Geothermal Research*, 119(1–4), 241–254.
- Hashimoto, T., Koyama, T., Kaneko, T., Ohminato, T., Yanagisawa, T., Yoshimoto, M., & Suzuki, E. (2014). Aeromagnetic survey using an unmanned autonomous helicopter over Tarumae volcano, northern Japan. *Exploration Geophysics*, 45, 37–42. <https://doi.org/10.1071/EG12087>
- Hickey-Vargas, R., López-Escobar, L., Moreno, H., Clavero, J., Lara, L., & Sun, M. (2004). Magmatic evolution of the villarrica volcano. In L. E. Lara & J. Clavero (Eds.), *Villarrica Volcano (39.5°S), southern Andes, Chile* (Bol. 61, pp. 39–45). Santiago, Chile: Serv. Nac. de Geol. y Miner.
- Holland, A. P., Watson, I. M., Phillips, J. C., Caricchi, L., & Dalton, M. P. (2011). Degassing processes during lava dome growth: Insights from Santiaguito lava dome, Guatemala. *Journal of Volcanology and Geothermal Research*, 202(1–2), 153–166. <https://doi.org/10.1016/j.jvolgeores.2011.02.004>
- Horton, K. A., Williams-Jones, G., Garbeil, H., Elias, T., Sutton, A. J., Mouginiis-Mark, P., et al. (2006). Real-time measurement of volcanic SO<sub>2</sub> emissions: Validation of a new UV correlation spectrometer (FLYSPEC). *Bulletin of Volcanology*, 68, 323–327. <https://doi.org/10.1007/s00445-005-0014-9>
- Ilanko, T., Oppenheimer, C., Burgisser, A., & Kyle, P. (2015). Cyclic degassing of Erebus volcano, Antarctica. *Bulletin of Volcanology*, 77, 56. <https://doi.org/10.1007/s00445-015-0941-z>
- Jacques, G., Hoernle, K., Gill, J., Hauff, F., Wehrmann, H., Garbe-Schönberg, D., et al. (2013). Across-arc geochemical variations in the Southern Volcanic Zone, Chile (34.5–38.0°S): Constraints on mantle wedge and slab input compositions. *Geochimica et Cosmochimica Acta*, 123, 218–243. <https://doi.org/10.1016/j.gca.2013.05.016>
- Johnson, J. B., Watson, L. M., Palma, J. L., Dunham, E. M., & Anderson, J. F. (2018). Forecasting the eruption of an open-vent volcano using resonant infrasound tones. *Geophysical Research Letters*, 45, 2213–2220. <https://doi.org/10.1002/2017GL076506>
- Kaneko, T., Koyama, T., Yasuda, A., Takeo, M., Yanagisawa, T., Kajiwara, K., & Honda, Y. (2011). Low-altitude remote sensing of volcanoes using an unmanned autonomous helicopter: An example of aeromagnetic observation at Izu-Oshima volcano, Japan. *International Journal of Remote Sensing*, 32, 1491–1504. <https://doi.org/10.1080/01431160903559770>
- Kantzas, E. P., McGonigle, A. J. S., Tamburello, G., Aiuppa, A., & Bryant, R. G. (2010). Protocols for UV camera volcanic SO<sub>2</sub> measurements. *Journal of Volcanology and Geothermal Research*, 194, 55–60. <https://doi.org/10.1016/j.jvolgeores.2010.05.003>
- Kelly, P. (2017). On the accuracy and precision of multi-GAS measurements, Proc. 13th CCVG-IAVCEI gas workshop, Ecuador.
- Koyama, T., Kaneko, T., Ohminato, T., Yanagisawa, T., Watanabe, A., & Takeo, M. (2013). An aeromagnetic survey of Shinmoe-dake volcano, Kirishima, Japan, after the 2011 eruption using an unmanned autonomous helicopter. *Earth, Planets and Space*, 65, 657–666. <https://doi.org/10.5047/eps.2013.03.005>

- Lamb, O. D., Varley, N. R., Mather, T. A., Pyle, D. M., Smith, P. J., & Liu, E. J. (2014). Multiple timescales of cyclical behaviour observed at two dome-forming eruptions. *Journal of Volcanology and Geothermal Research*, 284, 106–121. <https://doi.org/10.1016/j.jvolgeores.2014.07.013>
- Mason, E., Edmonds, M., & Turchyn, A. V. (2017). Remobilization of crustal carbon may dominate volcanic arc emissions. *Science*, 357, 290–294. <https://doi.org/10.1126/science.aan5049>
- Mather, T. A., Tsanev, V. I., Pyle, D. M., McGonigle, A. J. S., Oppenheimer, C., & Allen, A. G. (2004). Characterization and evolution of tropospheric plumes from Lascar and Villarrica volcanoes, Chile. *Journal of Geophysical Research*, 109, D21303. <https://doi.org/10.1029/2004JD004934>
- McGonigle, A. J. S., Aiuppa, A., Giudice, G., Tamburello, G., Hodson, A. J., & Gurrieri, S. (2008). Unmanned aerial vehicle measurements of volcanic carbon dioxide fluxes. *Geophysical Research Letters*, 35, L06303. <https://doi.org/10.1029/2007GL032508>
- McGonigle, A. J. S., Oppenheimer, C., Galle, B., Mather, T. A., & Pyle, D. M. (2002). Walking traverse and scanning DOAS measurements of volcanic gas emission rates. *Geophysical Research Letters*, 29(29), 1985. <https://doi.org/10.1029/2002GL015827>
- McGonigle, A. J. S., Oppenheimer, C., Hayes, A. R., Galle, B., Edmonds, M., Caltabiano, T., et al. (2003). Sulphur dioxide fluxes from Mount Etna, Vulcano, and Stromboli measured with an automated scanning ultraviolet spectrometer. *Journal of Geophysical Research*, 108, 2455. <https://doi.org/10.1029/2002JB002261>
- McGonigle, A. J. S., Pering, T. D., Wilkes, T. C., Tamburello, G., D'Aleo, R., Bitetto, M., et al. (2017). Ultraviolet imaging of volcanic plumes: A new paradigm in volcanology. *Geosciences*, 7, 68. <https://doi.org/10.3390/geosciences7030068>
- Moffat, A. J., & Millan, M. M. (1971). The applications of optical correlation techniques to the remote sensing of SO<sub>2</sub> plumes using sky light. *Atmospheric Environment* (1967), 5, 677–690. [https://doi.org/10.1016/0004-6981\(71\)90125-9](https://doi.org/10.1016/0004-6981(71)90125-9)
- Moreno, H., Clavero, J., & Lara, L. (1994). Explosive post-glacial activity of Villarrica volcano, southern Andes. Paper presented at 7th Congreso Geológico Chileno, University of Concepcion, Concepcion, Chile.
- Mori, T., & Burton, M. (2006). The SO<sub>2</sub> camera: A simple, fast and cheap method for ground-based imaging of SO<sub>2</sub> in volcanic plumes. *Geophysical Research Letters*, 33, L24804. <https://doi.org/10.1029/2006GL027916>
- Mori, T., Hashimoto, T., Terada, A., Yoshimoto, M., Kazahaya, R., Shinohara, H., & Tanaka, R. (2016). Volcanic plume measurements using a UAV for the 2014 Mt. Ontake eruption. *Earth, Planets and Space*, 68, 49. <https://doi.org/10.1186/s40623-016-0418-0>
- Morlet, J., Arens, G., Fourgeau, E., & Glard, D. (1982). Wave propagation and sampling theory—Part I: Complex signal and scattering in multilayered media. *Geophysics*, 47, 203–221. <https://doi.org/10.1190/1.1441328>
- Moussallam, Y., Bani, P., Curtis, A., Barnie, T., Moussallam, M., Peters, N., et al. (2016). Sustaining persistent lava lakes: Observations from high-resolution gas measurements at Villarrica volcano, Chile. *Earth and Planetary Science Letters*, 454, 237–247. <https://doi.org/10.1016/j.epsl.2016.09.012>
- Müller, D., Walter, T. R., Schöpa, A., Witt, T., Steinke, B., Gudmundsson, M. T., & Dürig, T. (2017). High-resolution digital elevation modeling from TLS and UAV campaign reveals structural complexity at the 2014/2015 Holuhraun Eruption Site, Iceland. *Frontiers in Earth Science*, 5. <https://doi.org/10.3389/feart.2017.00059>
- Nakano, T., Kamiya, I., Tobita, M., Iwahashi, J., & Nakajima, H. (2014). Landform monitoring in active volcano by UAV and SfM-MVS technique. In *The international archives of photogrammetry, remote sensing and spatial information sciences; Gottingen* (pp. 71–75). Gottingen, Germany: Copernicus GmbH. <https://doi.org/10.5194/isprsarchives-XL-8-71-2014>
- Nicholson, E. J., Mather, T. A., Pyle, D. M., Odbert, H. M., & Christopher, T. (2013). Cyclical patterns in volcanic degassing revealed by SO<sub>2</sub> flux timeseries analysis: An application to Soufrière Hills volcano, Montserrat. *Earth and Planetary Science Letters*, 375, 209–221. <https://doi.org/10.1016/j.epsl.2013.05.032>
- Odbert, H. M., Stewart, R. C., & Wadge, G. (2014). Cyclic phenomena at the Soufrière Hills volcano, Montserrat. *Geological Society, London, Memoirs*, 39, 41–60. <https://doi.org/10.1144/M39.2>
- Odbert, H. M., & Wadge, G. (2009). Time series analysis of lava flux. *Journal of Volcanology and Geothermal Research*, 188, 305–314. <https://doi.org/10.1016/j.jvolgeores.2009.09.005>
- Oppenheimer, C., Francis, P., & Stix, J. (1998). Depletion rates of sulfur dioxide in tropospheric volcanic plumes. *Geophysical Research Letters*, 25, 2671–2674. <https://doi.org/10.1029/98GL01988>
- OVDAS Reporte Especial de Actividad Volcánica (2017). Región de La Araucanía y Los Ríos, 05 December 2017, 09:50.
- Palma, J. L., Calder, E. S., Basualto, D., Blake, S., & Rothery, D. A. (2008). Correlations between SO<sub>2</sub> flux, seismicity, and outgassing activity at the open vent of Villarrica volcano, Chile. *Journal of Geophysical Research*, 113, B10201. <https://doi.org/10.1029/2008JB005577>
- Parejas, C. S., Druitt, T. H., Robin, C., Moreno, H., & Naranjo, J.-A. (2010). The Holocene Pucón eruption of Volcán Villarrica, Chile: Deposit architecture and eruption chronology. *Bulletin of Volcanology*, 72, 677–692. <https://doi.org/10.1007/s00445-010-0348-9>
- Percival, D. B., & Walden, A. T. (1993). *Spectral analysis for physical applications*. Cambridge, UK: Cambridge University Press. <https://doi.org/10.1017/CBO9780511622762>
- Percival, D. B., & Walden, A. T. (2006). *Wavelet methods for time series analysis*. Cambridge: Cambridge University Press.
- Pering, T. D., Tamburello, G., McGonigle, A. J. S., Aiuppa, A., Cannata, A., Giudice, G., & Patané, D. (2014). High time resolution fluctuations in volcanic carbon dioxide degassing from Mount Etna. *Journal of Volcanology and Geothermal Research*, 270, 115–121. <https://doi.org/10.1016/j.jvolgeores.2013.11.014>
- Pering, T. D., Tamburello, G., McGonigle, A. J. S., Hanna, E., & Aiuppa, A. (2014). Correlation of oscillatory behaviour in Matlab using wavelets. *Computers & Geosciences*, 70, 206–212. <https://doi.org/10.1016/j.cageo.2014.06.006>
- Peters, N., Hoffmann, A., Barnie, T., Herzog, M., & Oppenheimer, C. (2015). Use of motion estimation algorithms for improved flux measurements using SO<sub>2</sub> cameras. *Journal of Volcanology and Geothermal Research*, 300, 58–69. <https://doi.org/10.1016/j.jvolgeores.2014.08.031>
- Peters, N., & Oppenheimer, C. (2018). Plumetrack: Flux calculation software for UV cameras. *Computers & Geosciences*, 118, 86–90. <https://doi.org/10.1016/j.cageo.2018.05.014>
- Pieri, D., Diaz, J. A., Bland, G., Fladeland, M., Madrigal, Y., Corrales, E., et al. (2013). In situ observations and sampling of volcanic emissions with NASA and UCR unmanned aircraft, including a case study at Turrialba volcano, Costa Rica. *Geological Society, London, Special Publications*, 380, 321–352. <https://doi.org/10.1144/SP380.13>
- Platt, U., Bobrowski, N., Butz, A., Platt, U., Bobrowski, N., & Butz, A. (2018). Ground-based remote sensing and imaging of volcanic gases and quantitative determination of multi-species emission fluxes. *Geosciences*, 8, 44. <https://doi.org/10.3390/geosciences8020044>
- Richardson, J. P., Waite, G. P., & Palma, J. L. (2014). Varying seismic-acoustic properties of the fluctuating lava lake at Villarrica volcano, Chile. *Journal of Geophysical Research: Solid Earth*, 119, 5560–5573. <https://doi.org/10.1002/2014JB011002>
- Roberts, T. J., Lurton, T., Giudice, G., Liuzzo, M., Aiuppa, A., Coltelli, M., et al. (2017). Validation of a novel Multi-Gas sensor for volcanic HCl alongside H<sub>2</sub>S and SO<sub>2</sub> at Mt. Etna. *Bulletin of Volcanology*, 79, 36. <https://doi.org/10.1007/s00445-017-1114-z>



- Rüdiger, J., Tirpitz, J.-L., de Moor, J. M., Bobrowski, N., Gutmann, A., Liuzzo, M., et al. (2018). Implementation of electrochemical, optical and denuder-based sensors and sampling techniques on UAV for volcanic gas measurements: Examples from Masaya, Turrialba and Stromboli volcanoes. *Atmospheric Measurement Techniques*, *11*, 2441–2457. <https://doi.org/10.5194/amt-11-2441-2018>
- Santoro, S., Parracino, S., Fiorani, L., D'Aleo, R., Di Ferdinando, E., Giudice, G., et al. (2017). Volcanic plume CO<sub>2</sub> flux measurements at Mount Etna by mobile differential absorption Lidar. *Geosciences*, *7*, 9. <https://doi.org/10.3390/geosciences7010009>
- Sawyer, G. M., Salerno, G. G., Le Blond, J. S., Martin, R. S., Spampinato, L., Roberts, T. J., et al. (2011). Gas and aerosol emissions from Villarrica volcano, Chile. *Journal of Volcanology and Geothermal Research*, *203*, 62–75. <https://doi.org/10.1016/j.jvolgeores.2011.04.003>
- Shinohara, H. (2005). A new technique to estimate volcanic gas composition: Plume measurements with a portable multi-sensor system. *Journal of Volcanology and Geothermal Research*, *143*, 319–333. <https://doi.org/10.1016/j.jvolgeores.2004.12.004>
- Shinohara, H. (2013). Composition of volcanic gases emitted during repeating Vulcanian eruption stage of Shinmoedake, Kirishima volcano, Japan. *Earth, Planets and Space*, *65*, 667–675. <https://doi.org/10.5047/eps.2012.11.001>
- Shinohara, H., Aiuppa, A., Giudice, G., Gurrieri, S., & Liuzzo, M. (2008). Variation of H<sub>2</sub>O/CO<sub>2</sub> and CO<sub>2</sub>/SO<sub>2</sub> ratios of volcanic gases discharged by continuous degassing of Mount Etna volcano, Italy. *Journal of Geophysical Research*, *113*, B09203. <https://doi.org/10.1029/2007JB005185>
- Shinohara, H., & Witter, J. B. (2005). Volcanic gases emitted during mild Strombolian activity of Villarrica volcano, Chile. *Geophysical Research Letters*, *32*, L20308. <https://doi.org/10.1029/2005GL024131>
- Stix, J., de Moor, J. M., Rüdiger, J., Alan, A., Corrales, E., D'Arcy, F., et al. (2018). Using drones and miniaturized instrumentation to study degassing at Turrialba and Masaya volcanoes, Central America. *Journal of Geophysical Research: Solid Earth*, *123*, 6501–6520. <https://doi.org/10.1029/2018JB015655>
- Tamburello, G. (2015). Ratiocalc: Software for processing data from multicomponent volcanic gas analyzers. *Computers & Geosciences*, *82*, 63–67. <https://doi.org/10.1016/j.cageo.2015.05.004>
- Tamburello, G., Aiuppa, A., Kantzas, E. P., McGonigle, A. J. S., & Ripepe, M. (2012). Passive vs. active degassing modes at an open-vent volcano (Stromboli, Italy). *Earth and Planetary Science Letters*, *359–360*, 106–116. <https://doi.org/10.1016/j.epsl.2012.09.050>
- Tamburello, G., Aiuppa, A., McGonigle, A. J. S., Allard, P., Cannata, A., Giudice, G., et al. (2013). Periodic volcanic degassing behavior: The Mount Etna example. *Geophysical Research Letters*, *40*, 4818–4822. <https://doi.org/10.1002/grl.50924>
- Thompson, D. (1982). Spectrum estimation and harmonic analysis. *Proceedings of the IEEE*, *70*, 1055–1096.
- Torrence, C., & Compo, G. P. (1998). A practical guide to wavelet analysis. *Bulletin of the American Meteorological Society*, *79*, 61–78. <https://doi.org/10.1175/1520-0477>
- Turner, N. R., Perroy, R. L., & Hon, K. (2017). Lava flow hazard prediction and monitoring with UAS: A case study from the 2014–2015 Pāhoa lava flow crisis, Hawai'i. *Journal of Applied Volcanology*, *6*, 17. <https://doi.org/10.1186/s13617-017-0068-3>
- Wehrmann, H., Hoernle, K., Jacques, G., Garbe-Schönberg, D., Schumann, K., Mahlke, J., & Lara, L. E. (2014). Volatile (sulphur and chlorine), major, and trace element geochemistry of mafic to intermediate tephra from the Chilean Southern Volcanic Zone (33–43°S). *International Journal of Earth Sciences*, *103*, 1945–1962. <https://doi.org/10.1007/s00531-014-1006-9>
- Weibring, P., Edner, H., Svanberg, S., Cecchi, G., Pantani, L., Ferrara, R., & Caltabiano, T. (1998). Monitoring of volcanic sulphur dioxide emissions using differential absorption lidar (DIAL), differential optical absorption spectroscopy (DOAS), and correlation spectroscopy (COSPEC). *Applied Physics B: Lasers and Optics*, *67*, 419–426. <https://doi.org/10.1007/s003400050525>
- Werner, C., Hurst, T., Scott, B., Sherburn, S., Christenson, B. W., Britten, K., et al. (2008). Variability of passive gas emissions, seismicity, and deformation during crater lake growth at White Island volcano, New Zealand, 2002–2006. *Journal of Geophysical Research*, *113*, B01204. <https://doi.org/10.1029/2007JB005094>
- Wilkes, T. C., McGonigle, A. J. S., Pering, T. D., Taggart, A. J., White, B. S., Bryant, R. G., & Willmott, J. R. (2016). Ultraviolet imaging with low cost smartphone sensors: Development and application of a raspberry Pi-based UV camera. *Sensors*, *16*, 1649. <https://doi.org/10.3390/s16101649>
- Wilkes, T. C., Pering, T. D., McGonigle, A. J. S., Tamburello, G., & Willmott, J. R. (2017). A low-cost smartphone sensor-based UV camera for volcanic SO<sub>2</sub> emission measurements. *Remote Sensing*, *9*, 27. <https://doi.org/10.3390/rs9010027>
- Witter, J. B., Kress, V. C., Delmelle, P., & Stix, J. (2004). Volatile degassing, petrology, and magma dynamics of the Villarrica Lava Lake, Southern Chile. *Journal of Volcanology and Geothermal Research*, *134*(4), 303–337.
- Xi, X., Johnson, M. S., Jeong, S., Fladeland, M., Pieri, D., Diaz, J. A., & Bland, G. L. (2016). Constraining the sulfur dioxide degassing flux from Turrialba volcano, Costa Rica using unmanned aerial system measurements. *Journal of Volcanology and Geothermal Research*, *325*, 110–118. <https://doi.org/10.1016/j.jvolgeores.2016.06.023>